7. H. Huang, S. C. Yin, L. F. Nazar, *Electrochem. Solid-State Lett.* **4**, A170–A172 (2001).
8. E. S. Takeuchi *et al.*, *Chem. Mater.* **21**, 4934–4939 (2009).
9. E. S. Takeuchi *et al.*, *J. Solid State Chem.* **200**, 232–240 (2013).
10. E. S. Takeuchi *et al.*, *Energy Environ. Sci.* **6**, 1465–1470 (2013).
11. F. Sauvage, V. Bodenez, J. M. Tarascon, K. R. Poeppelmeier, *Inorg. Chem.* **49**, 6461–6467 (2010).
12. K. C. Kirshenbaum *et al.*, *Phys. Chem. Chem. Phys.* **16**, 9138–9147 (2014).
13. J. Rijssenbeek *et al.*, *J. Power Sources* **196**, 2332–2339 (2011).
14. M. Ebner, F. Marone, M. Stampanoni, V. Wood, *Science* **342**, 716–720 (2013).
15. D. C. Bock, K. J. Takeuchi, A. C. Marschilok, E. S. Takeuchi, *Dalton Trans.* **42**, 13981–13989 (2013).
16. A. C. Marschilok *et al.*, *J. Power Sources* **195**, 6839–6846 (2010).
17. R. A. Leising, W. C. Thiebolt, E. S. Takeuchi, *Inorg. Chem.* **33**, 5733–5740 (1994).
18. F. Sauvage *et al.*, *Inorg. Chem.* **47**, 8464–8472 (2008).
19. S. Calvin, in *XAFS for Everyone* (CRC Press, Boca Raton, FL, 2013), p. xxvi.
20. C. J. Patridge *et al.*, *J. Phys. Chem. C* **115**, 14437–14447 (2011).
21. P. Chaurand *et al.*, *J. Phys. Chem. B* **111**, 5101–5110 (2007).
22. J. Wong, F. W. Lytle, R. P. Messmer, D. H. Maylotte, *Phys. Rev. B* **30**, 5596–5610 (1984).
23. P. E. Stallworth, S. Kostov, M. L. denBoer, S. G. Greenbaum, C. Lampe-Onnerud, *J. Appl. Phys.* **83**, 1247–1255 (1998).

MATERIALS SCIENCE

Assembly of micro/nanomaterials into complex, three-dimensional architectures by compressive buckling

Sheng Xu,[1]* Zheng Yan,[1]* Kyung-In Jang,[1] Wen Huang,[2] Haoran Fu,[3,4] Jeonghyun Kim,[1,5] Zijun Wei,[1] Matthew Flavin,[1] Joselle McCracken,[6] Renhan Wang,[1] Adina Badea,[6] Yuhao Liu,[1] Dongqing Xiao,[6] Guoyan Zhou,[3,7] Jungwoo Lee,[1,5] Ha Uk Chung,[1] Huanyu Cheng,[1,3] Wen Ren,[6] Anthony Banks,[1] Xiuling Li,[2] Ungyu Paik,[5] Ralph G. Nuzzo,[1,6] Yonggang Huang,[3]† Yihui Zhang,[3,8]† John A. Rogers[1,2,6,9]†

Complex three-dimensional (3D) structures in biology (e.g., cytoskeletal webs, neural circuits, and vasculature networks) form naturally to provide essential functions in even the most basic forms of life. Compelling opportunities exist for analogous 3D architectures in human-made devices, but design options are constrained by existing capabilities in materials growth and assembly. We report routes to previously inaccessible classes of 3D constructs in advanced materials, including device-grade silicon. The schemes involve geometric transformation of 2D micro/nanostructures into extended 3D layouts by compressive buckling. Demonstrations include experimental and theoretical studies of more than 40 representative geometries, from single and multiple helices, toroids, and conical spirals to structures that resemble spherical baskets, cuboid cages, starbursts, flowers, scaffolds, fences, and frameworks, each with single- and/or multiple-level configurations.

Controlled formation of 3D functional meso-structures is a topic of broad and increasing interest, particularly in the past decade (*1–9*). Uses of such structures have been envisioned in nearly every type of micro/nanosystem technology, including biomedical devices (*10–12*), microelectromechanical components (*13, 14*), photonics and optoelectronics (*15–17*), metamaterials (*16, 18–21*), electronics (*22, 23*), and energy storage (*24, 25*). Although volumetric optical exposures (*4, 6, 19*), fluidic self-assembly (*3, 26, 27*), residual stress-induced bending (*1, 13, 21, 28–31*), and templated growth (*7, 8, 32*) can be used to realize certain classes of structures in certain types of materials, techniques that rely on rastering of fluid nozzles or focused beams of light provide the greatest versatility in design (*5, 6*). The applicability of these latter methods, however, only extends directly to materials that can be formulated as inks or patterned by exposure to light or other energy sources, and indirectly to those that can be depo-

sited onto or into sacrificial 3D structures formed with these materials (*5, 6, 18, 19*). Integration of more than one type of any material into a single structure can be challenging. Furthermore, the serial nature of these processes sets practical constraints on operating speeds and overall addressable areas. These and other limitations stand in stark contrast with the exceptional fabrication capabilities that exist for the types of planar micro/nanodevices that are ubiquitous in state-of-the-art semiconductor technologies. Routes to 3D mesostructures that exploit this existing base of competencies can provide options in high-performance function that would otherwise be unobtainable.

Methods based on residual stress-induced bending are naturally compatible with modern planar technologies, and they offer yields and throughputs necessary for practical applications. Such schemes provide access to only certain classes of geometries, through either rotations of rigid plates to yield tilted panels,

rectangular cuboids, pyramids, or other hollow polyhedra, or rolling motions of flexible films to form tubes, scrolls, or related shapes with cylindrical symmetry [for reviews, see (*1, 9, 13*)]. Here, we present a different set of concepts in which strain relaxation in an elastomeric substrate simultaneously imparts forces at a collection of lithographically controlled locations on the surfaces of planar precursor structures. The resulting processes of controlled, compressive buckling induce rapid, large-area geometric extension into the third dimension, capable of transforming the most advanced functional materials and planar microsystems into mechanically tunable 3D forms with broad geometric diversity.

As a simple illustrative example, we present results of finite-element analyses (FEAs) (*33*) of the steps for assembly of a pair of 3D conical helices made of monocrystalline silicon in Fig. 1A. The process begins with planar micro/nanofabrication of 2D filamentary serpentine silicon ribbons (2 μm thick, 60 μm wide), with spatial gradients in their arc radii. Lithographically defined exposure of these structures to ozone formed using ultraviolet light creates precisely controlled patterns of surface hydroxyl terminations at strategic locations (red dots in Fig. 1A) along their lengths. A soft silicone
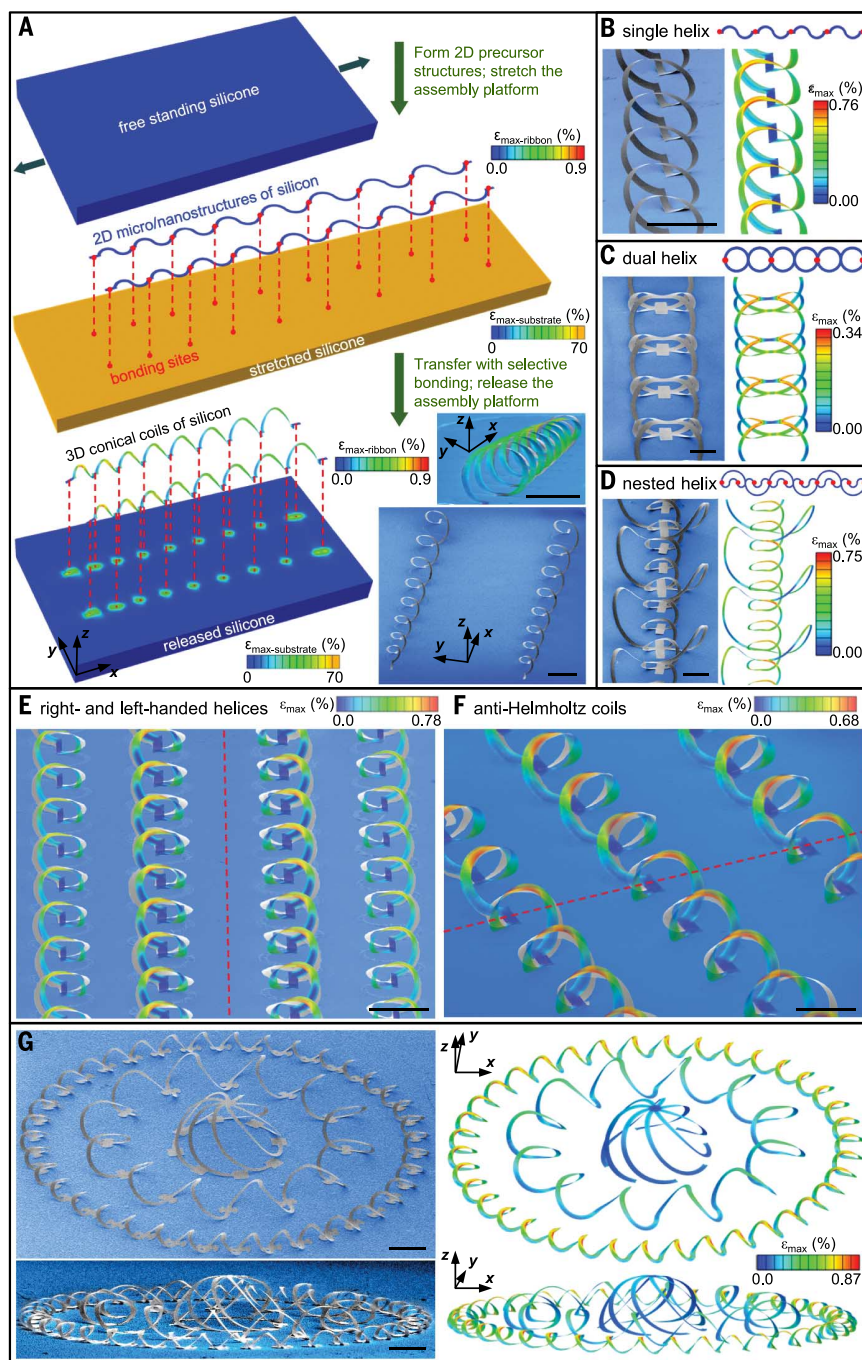
[1]Department of Materials Science and Engineering and Frederick Seitz Materials Research Laboratory, University of Illinois at Urbana-Champaign, Urbana, IL 61801, USA. [2]Department of Electrical and Computer Engineering, University of Illinois at Urbana-Champaign, Urbana, IL 61801, USA. [3]Department of Civil and Environmental Engineering and Department of Mechanical Engineering, Center for Engineering and Health, and Skin Disease Research Center, Northwestern University, Evanston, IL 60208, USA. [4]Department of Civil Engineering and Architecture, Zhejiang University, Hangzhou 310058, P.R. China. [5]Department of Materials Science and Engineering, Department of Energy Engineering, Hanyang University, Seoul 133-791, Republic of Korea. [6]Department of Chemistry, University of Illinois at Urbana, Urbana, IL 61801, USA. [7]Key Laboratory of Pressure Systems and Safety (MOE), School of Mechanical and Power Engineering, East China University of Science and Technology, Shanghai 200237, P.R. China. [8]Center for Mechanics and Materials, Tsinghua University, Beijing 100084, P.R. China. [9]Beckman Institute for Advanced Science and Technology, University of Illinois at Urbana-Champaign, Urbana, IL 61801, USA.
*These authors contributed equally to this work. †Corresponding author. E-mail: jrogers@illinois.edu (J.A.R.); y-huang@northwestern.edu (Y.H.); yihui.zhang2011@gmail.com (Y.Z.)

A free standing silicone

Form 2D precursor structures; stretch the assembly platform

2D micro/nanostructures of silicon

$\varepsilon_{\text{max-ribbon}}$ (%)
0.0   0.9

bonding sites   stretched silicone

$\varepsilon_{\text{max-substrate}}$ (%)
0   70

Transfer with selective bonding; release the assembly platform

3D conical coils of silicon

$\varepsilon_{\text{max-ribbon}}$ (%)
0.0   0.9

released silicone

$\varepsilon_{\text{max-substrate}}$ (%)
0   70

B single helix
ε_{max} (%)
0.76
0.00

C dual helix
ε_{max} (%)
0.34
0.00

D nested helix
ε_{max} (%)
0.75
0.00

E right- and left-handed helices ε_{max} (%) 0.0 0.78

F anti-Helmholtz coils ε_{max} (%) 0.0 0.68

G ε_{max} (%) 0.0 0.87

Fig. 1. Process for deterministic assembly of 3D mesostructures of monocrystalline silicon from 2D precursors. (**A**) Finite-element analysis (FEA) results that correspond to the formation of 3D conical helices from 2D filamentary serpentine ribbons of silicon bonded at selected points (red dots) to a stretched slab of silicone elastomer. Compressive forces induced by relaxing the strain in the elastomer lead to coordinated out-of-plane buckling, twisting, and translational motions in the silicon, yielding 3D mesostructures. The scanning electron microscope (SEM) images at the lower right show an experimental result. (**B**) Schematic diagram of a 2D silicon precursor and its bonding sites (top), an SEM image of a single-helical coil formed from this precursor (left), and corresponding FEA prediction (right). (**C** and **D**) Similar results for a dual-helix coil (C) and a nested, coaxial pair of connected helical coils (D). (**E**) SEM image with overlaid FEA prediction of helical coils with right- and left-handed chirality, on the left and right sides of the dashed red line, respectively. (**F**) SEM image with overlaid FEA prediction of structures whose chirality changes abruptly at the locations defined by the dashed red line. (**G**) SEM images and FEA predictions of a complex 3D mesostructure formed from a 2D precursor that consists of closed-loop circular filamentary serpentines and radially oriented ribbons, selectively bonded to a biaxially stretched elastomer substrate. In all cases, the color in the FEA results corresponds to the maximum principal strains. Scale bars, 400 μm.

elastomer substrate (Dragon Skin; Smooth-On, Easton, PA) that is uniaxially stretched to a large level of prestrain ($\varepsilon_{\text{pre}} = \Delta L/L$, where ΔL is the increase in length and is comparable to or larger than L; $\varepsilon_{\text{pre}} \approx 70\%$ for the case shown here) and is then exposed to ozone to generate a uniform coverage of surface hydroxyl groups serves as a platform that guides the mechanical assembly process. Transfer printing of the 2D serpentines onto this surface leads to strong, spatially selective bonding [work of adhesion >8 J/m² (*33*)] via covalent linkages that form upon contact as a result of condensation reactions at the regions of the silicon that present hydroxyl groups (*34, 35*). Comparatively weak van der Waals forces dominate interfacial interactions at all other locations [work of adhesion ~0.2 J/m² (*36*)].

Allowing the substrate to return to its original shape induces large compressive forces on the serpentine precursors. Forces above a certain threshold initiate a controlled buckling process that lifts the weakly bonded regions of the serpentines out of contact with the substrate surface and, at the same time, induces spatially dependent deformations (in terms of twisting and bending) and in- and out-of-plane translations. The 3D structures involve a balance between the forces of adhesion to the substrate and the strain energies of the bent, twisted ribbons. The latter (W_{strain}) depends on the elastic modulus (E) and the thickness (t) and lateral dimension (w) of the ribbons via a simple scaling law, $W_{\text{strain}} \propto Ewt^3$. The 3D structures formed by these correlated motions represent self-supporting frameworks that remain tethered to the assembly platform at the covalent bonding sites. This process leaves residual strains in the substrate that are negligible everywhere except for the immediate vicinity of these sites, as well as strains in the silicon that are well below fracture thresholds (Fig. 1A). This mechanically guided, deterministic process of geometric transformation from 2D to 3D is governed by (i) the 2D layout of the precursor materials, their dimensions and mechanical properties; (ii) the pattern of sites for selective bonding; and (iii) the nature and magnitude of the prestrain in the assembly platform. The resulting 3D structures differ qualitatively from surface buckling or wrinkling patterns that can occur in thin films [e.g., (*37–39*)]. Quantitative analysis captures all of these aspects, as illustrated by the excellent agreement between experiment and computation in Fig. 1A and fig. S1. The coils shown here have eight turns, with a pitch (i.e., dimension along x axis) that varies gradually from ~454 μm to ~817 μm, a width (i.e., dimension along y axis) from ~252 μm to ~474 μm, and a height (i.e., dimension along z axis) from ~240 μm to ~459 μm. The relative differences between the experimentally observed structural geometries and those from FEA predictions are <8.5%. See (*33*) and figs. S2 and S3 for detailed materials and fabrication procedures.

With this scheme, diverse feature sizes and wide-ranging geometries can be realized in many different classes of materials. A simple case related to that in Fig. 1A results from a precursor that

consists of a 2D serpentine ribbon in a spatially invariant periodic geometry (2 μm thick, 50 μm wide; schematic top-view illustration in the upper panel of Fig. 1B). Here, selective bonding to an assembly platform that is strained uniaxially to ε_{pre} = 90% yields a uniform, single-helical coil (Fig. 1B). The experimental results are in quantitative agreement with FEA (Fig. 1B and fig. S4) and with analytical parametric equations developed by exploring key characteristics of the deformations (33) (fig. S5). Such models establish the relationship between geometric configurations and ε_{pre}, indi-

cating that the heights of the helices increase with ε_{pre} while the widths remain largely unchanged, as might be expected. Modifying the structure of the 2D precursor within this theme while changing the distribution of the bonding sites enables access to dual helices (Fig. 1C), nested coaxial structures (Fig. 1D), helices with opposite chirality (Fig. 1E), and even structures whose chirality changes abruptly at selected locations (Fig. 1F). In all of the examples in Fig. 1, the maximum principal strains in the silicon (from ~0.34% to 0.90%) occur at locations of large changes in

curvature. Computational models provide quantitative guidance in the selection of designs that avoid strains at levels that could result in fracture of the constituent materials, localized deformation, or self-contact. For simple cases, some of these guidelines can be captured in analytical forms (33) (fig. S6). In single helices, the maximum strains increase linearly with both the thicknesses and widths of the 2D precursors, with greater sensitivity to the thickness.

The assembled structures are not restricted to geometries with axial symmetry. Joining

Fig. 2. Experimental and computational studies of various 3D mesostructures and classification according to their modes of deformation. (**A**) Average curvature components and mode ratio of a 3D mesostructure (3D wavy ribbon) that involves only bending, as a function of prestrain in the stretched assembly platform. (**B**) Similar results for a 3D mesostructure (3D single-helical coil) that involves both bending and twisting. Dots represent FEA results; solid lines represent the scaling law $\kappa_{bend}, \kappa_{twist} \propto \sqrt{\varepsilon_{compr}}$. The colors in the 3D FEA correspond to the maximum principal strains. (**C** and **D**) 2D precursors, mode ratios, optical micrographs, and FEA predictions for 18 3D mesostructures that exhibit bending-dominated modes (C) and bending-twisting mixed modes (D). Scale bars, 200 μm.

Mode ratio	2D precursor	3D structure (FEA)	3D structure (Experiment)
Tent R=0			
Table R=0			
Box I R=0			
Tilted table R=0.10			
Flower R=0.11			
Inverted flower R=0.12			
Two-layer flower R=0.14			
Rotated table R=0.15			
Box II R=0.16			

Mode ratio	2D precursor	3D structure (FEA)	3D structure (Experiment)
Folded box R=0.26			
Basket R=0.34			
Star R=0.36			
Butterfly R=0.45			
Starfish R=0.47			
Box with roof R=0.67			
Circular helix I R=0.89			
Circular helix II R=1.07			
Circular helix III R=1.09			

closed-form circular 2D serpentines with equally biaxially stretched assembly platforms (fig. S7) yields toroidal coils in isolation, in extended arrays, or in nested configurations. Figure 1G shows an elaborate 3D silicon mesostructure that consists of a concentric pair of toroids, with a separate hemispherical "cage" construct at the center; the corresponding 2D precursor is shown in fig. S8. The remarkably good agreement be-

tween experimental results and FEA predictions for this highly complex architecture provides further evidence of the fidelity of the assembly process and the accuracy of the models. The result is a deterministic route to 3D mesostructures with validated design tools that can assist in the selection of 2D precursor geometries, bonding sites, and stretching configurations for wide-ranging classes of topologies and architectures.

Dozens of basic 3D shapes, each identified with a descriptive name, are summarized in Fig. 2. A quantitative classification scheme follows from consideration of the buckling character-istics. In general, motions of ribbon-type pre-cursors (i.e., thickness t much smaller than width w) are dominated by out-of-plane bending and twisting deformations coupled with large-scale translational motion (fig. S9). By compari-son, in-plane bending is energetically unfavorable because the corresponding stiffness ($\propto w^3 t$) is much larger than that for out-of-plane bending or twisting ($\propto wt^3$). The magnitudes of bending and twisting deformations can be quantified by evaluating curvatures that are defined using a lo-cal coordinate system (fig. S9). The bending and torsional degrees of freedom of these developable ribbons are constrained by the isometric nature of the deformations (i.e., length invariant, as mea-sured along the central axes of the ribbons) as-sociated with formation of the 3D structures.

Buckling always involves considerable bending, whereas the amount of twisting depends strong-ly on the 2D structural details. One means of classification relies on a quantity, R, defined by the ratio of the average twisting curvature (κ_{twist}) to the average bending curvature (κ_{bend}), which can be determined by FEA (33). A given 3D meso-structure belongs to the bending-dominated mode when R, referred to as the mode ratio, is smaller than a critical value (e.g., 0.2 for the present pur-poses); otherwise, it belongs to the bending-twisting mixed mode. Representative examples presented in Fig. 2, A and B, fall into these two different regimes: a 3D wavy ribbon ($R = 0$) and a 3D helical coil ($R = 0.82$). The magnitudes of both κ_{twist} and κ_{bend} increase with compressive strain (ε_{compr}) applied to the 2D precursor, where $\varepsilon_{compr} = \varepsilon_{pre}/(1 + \varepsilon_{pre})$. Quantitative analyses show that both curvature components scale with the square root of ε_{compr}, thereby suggesting that R is independent of the compression level. This finding applies to all of the 3D mesostructures examined here, obtained with a diverse set of topologies and formed on assembly platforms with uniaxial as well as biaxial strains (Fig. 2, A and B, and figs. S10 and S11).

The layout of the 2D precursor and the con-figuration of the bonding sites both play crucial roles in determining the final 3D geometry (Fig. 2, C and D). With the same 2D precursor (e.g., the circular serpentine pattern or Kagome lattice), dif-ferent distributions of bonding sites yield different 3D configurations, with widely varying values of R. By comparison to these two factors, the cross-sectional dimensions (i.e., w and t) of the pre-cursor have minor effect. For 3D mesostructures that exhibit a bending-dominated mode (e.g., the flower and two-layer flower of Fig. 2C), R is insen-sitive to changes in the width or thickness (fig. S12). For bending-twisting mixed modes (e.g., straight helix in Fig. 1B and circular helix III in Fig. 2D), the width and thickness can lead to changes in R, but with magnitudes insufficient to induce a transition into the bending-dominated mode.

Multiple, hierarchical scales of buckling are also possible with the appropriate choice of design.
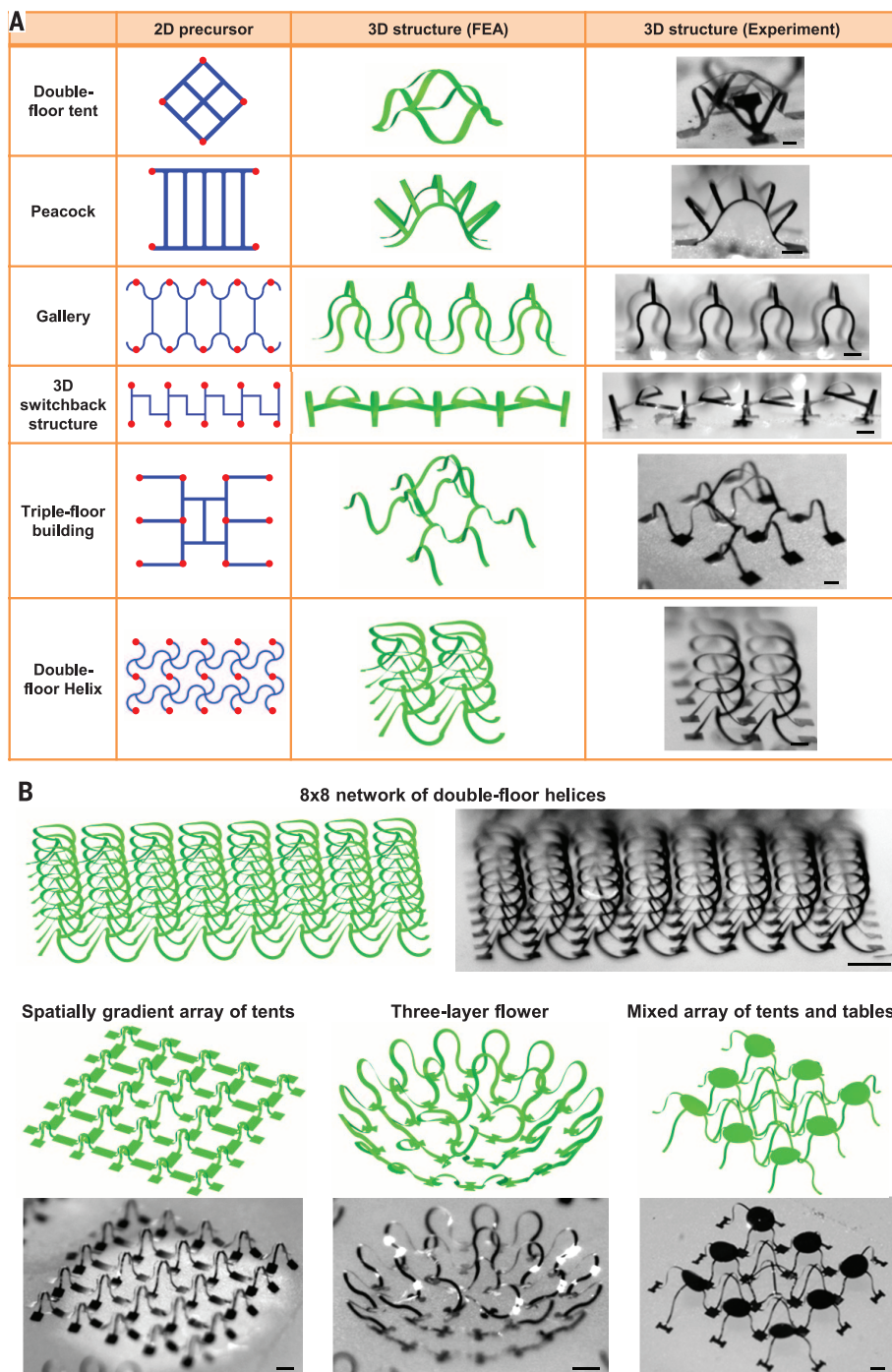
Fig. 3. 3D mesostructures with multilevel configurations and/or extended network architec-tures. (**A**) 2D precursors, FEA predictions, and optical micrographs for six 3D mesostructures that have double- or triple-level configurations. (**B**) Distributed 3D mesoscale networks comprising interconnected collections of the 3D structures in Figs. 2 and 3A. Scale bars, 200 μm (A), 400 μm (B).

Examples of 3D mesostructures that have multi-level constructions in the out-of-plane direction are presented in Fig. 3A. Such layouts can be achieved by adding filamentary ribbons to 2D precursors that yield single-level 3D shapes like those of Fig. 2. In the most extreme examples, these additional ribbons connect the precursor structures together at regions where the assembly process would otherwise yield the maximum out-of-plane displacements. Upon release of strain in the assembly platform, these ribbons—such as those that form the cross in the double-floor tent structure, the array of vertical ribbons in the peacock and gallery structures, or the horizontally aligned serpentine ribbons in the double-floor helix structure—undergo an additional level of buckling to form an elevated "second floor" suspended above the reach of buckling that represents the "first floor." This process substantially extends the maximum elevation above the substrate, thereby enhancing the 3D nature of the system. The triple-floor building structure provides a specific example. Here, the maximum out-of-plane displacement is ~1 mm for assembly using a biaxial prestrain of ~100%. This distance is up to ~2 times the maximum in-plane extent along the narrow dimension of the central part of the supporting structure.

The 3D mesostructures shown in Figs. 2 and 3A can be viewed as building blocks to yield large-scale, interconnected 3D mesoscale networks. The examples in Fig. 3B follow from repeating, mixing, joining, and/or nesting of these building blocks. The top frame shows an 8 × 8 array of the double-floor helix structure that consists of eight evenly spaced helices on the first floor and another eight helices, with the axial direction rotated by 90°, on the second floor (fig. S13). The lower left panel of Fig. 3B illustrates a 5 × 5 array of the 3D tent structure with a spatial gradient in the height, such that the largest tent appears at the center and smaller ones reside at the outermost peripheral regions. To its right is a dual, nested 3D flower structure with a fourfold symmetric toroid at the center. The rightmost example corresponds to a mixed array consisting of four regular table structures, four tilted tables, four tents, and one double-floor tent at the center. Some other 3D mesostructures (e.g., raised ring, scaffold, toroid inside a flower, nested box, etc.) appear in fig. S14. These networks exhibit geometries that agree quantitatively with FEA predictions. An important point is that all 3D mesostructures—even those with the highest complexity and largest extent in the out-of-plane direction—are deterministic and form consistently into unique geometries because the strain energies of the first-order buckling modes (i.e., energetically the most probable configuration) are lower than those of all other modes by approximately a factor of 2 or more (fig. S15).

Summarized in Fig. 4A and fig. S16 are results that illustrate the applicability of this assembly approach to additional classes of materials, including metals (e.g., Ni), dielectrics (e.g., polyimide and epoxy), and patterned combinations of these, in polycrystalline and amorphous forms. Submicrometer features are also possible, as demonstrated in a "starfish" framework that incorporates silicon ribbons with widths of 800 nm and thicknesses of 100 nm (Fig. 4B). Two more examples of submicrometer features are provided in fig. S17. Here, the large differences in contact areas between the filaments and the bonding sites provide the necessary contrast in adhesion. The same strategy also enables the assembly of micrometer-sized 3D silicon features with ribbon widths of 3 μm and thicknesses of 300 nm (fig. S18). In these and all other cases, mechanical strain applied to the assembly platforms can affect reversible, controlled changes in the geometries of the supported structures, thereby providing tunable 3D configurations. The results in Fig. 4C show top and angled views of the influence of uniaxial tensile deformation (50%) on a structure with a variant of the starfish layout, in which all six tip corners serve as sites for bonding. Overlaid FEA results exhibit quantitative agreement with the observed geometries. Results in fig. S19 demonstrate that the 3D mesostructures are bendable and can be placed on curved surfaces.
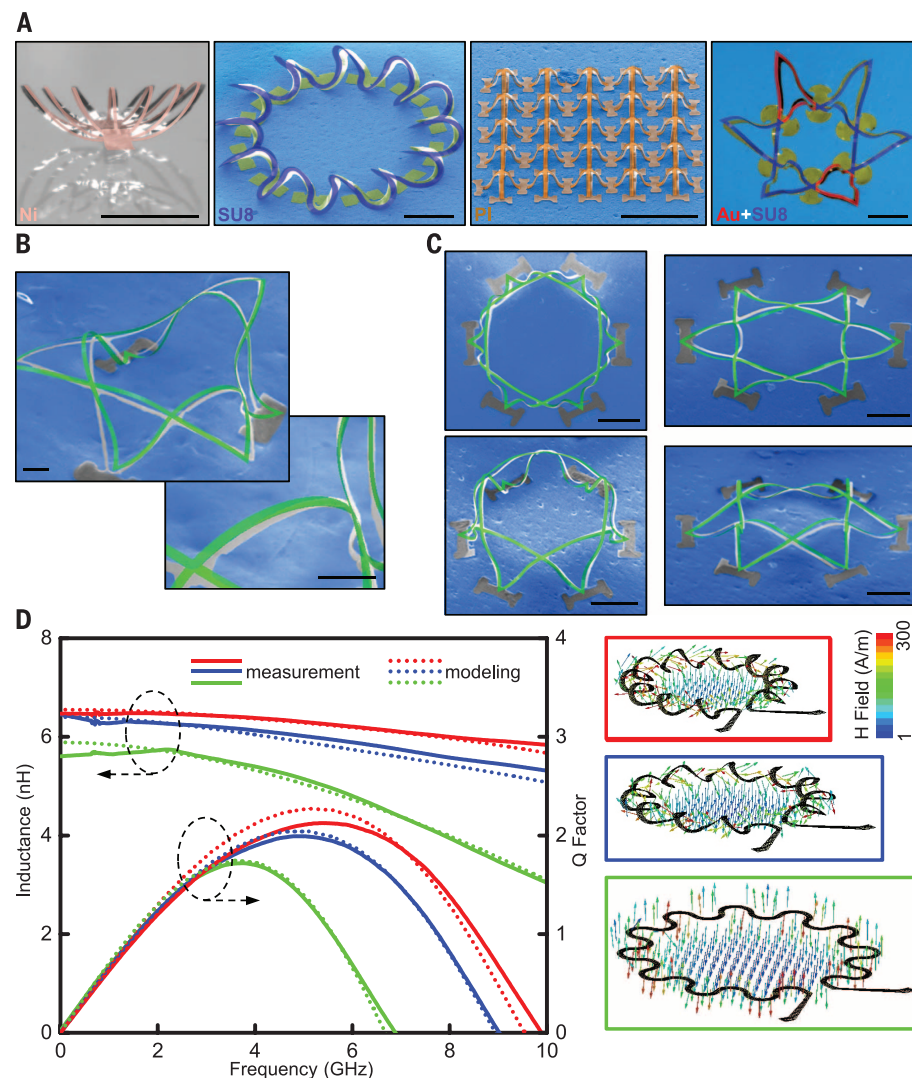
Fig. 4. 3D structures with various material compositions and feature sizes, and results for electrical behaviors in a tunable 3D toroidal inductor. (**A**) Experimental images and overlaid FEA predictions of 3D mesostructures made of metal (Ni), polymer [photodefinable epoxy (SU8) and polyimide (PI)], and heterogeneous combinations of materials (Au and SU8). Scale bars, 500 μm. (**B**) 3D mesostructures of silicon with lateral dimensions and thicknesses in the submicrometer regime, with overlaid FEA predictions. Scale bars, 5 μm. (**C**) 3D mesostructure of silicon in its as-fabricated state (left column) and in a configuration that results from uniaxially stretching the substrate (right column), all with overlaid FEA predictions. Scale bars, 50 μm. (**D**) Measured and computed frequency dependence of the inductance and the Q factor of a single 3D toroidal inductor mechanically configured into two different shapes by partial (21%, in an absolute sense, of an original prestrain of 54%; blue) and then complete release of prestrain (red), along with the corresponding 2D precursor (green) as reference. The panels on the right show simulated magnetic field distributions of these structures for feed-in power of 1 W. The arrows indicate direction and their colors indicate magnitude.

The ability to naturally integrate state-of-the-art electronic materials and devices represents an essential, defining characteristic of these approaches. A mechanically tunable inductor based on a 3D toroidal structure with feed and ground lines, all constructed with polyimide encapsulation (1.2 μm) and Ni conducting layers (400 nm), provides an example. Here, the geometry is similar to the "circular helix III" in Fig. 2D, with the addition of contact pads located at the periphery for electrical probing. The graph of Fig. 4D shows measurements and modeling results for the frequency dependence of the inductance and the quality (Q) factor for a 2D closed-loop serpentine precursor and a single 3D toroid structure in two different mechanically adjusted configurations. In both cases, the 3D cage structure enhances the mutual inductance between adjacent twisted turns. The maximum Q factors and resonant frequencies increase systematically from 1.7 to 2.2 GHz and from 6.8 to 9.5 GHz, respectively, as the structure transforms from 2D to two distinct 3D shapes associated with partial release (about half of the total initial prestrain of 54%) and then complete release of the prestrain. These trends arise from a systematic reduction in substrate parasitic capacitance with increasing three-dimensional character (40). The measured results correspond well to modeling that involves computation of the electromagnetic properties associated with the predicted 3D structure geometries from FEA, as shown in the right panels of Fig. 4D [see (33) and figs. S20 to S23].

The ideas presented here combine precise, lithographic control of the thicknesses, widths, and layouts of 2D structures with patterned sites of adhesion to the surfaces of high-elongation elastomer substrates to enable rapid assembly of broad classes of 3D mesostructures of relevance to diverse microsystem technologies. The process, which can be implemented with any substrate that is capable of controlled, large-scale dimensional change, expands and complements the capabilities of other approaches in 3D materials assembly. Compatibility with the most advanced materials (e.g., monocrystalline inorganics), fabrication methods (e.g., photolithography), and processing techniques (e.g., etching, deposition) that are available in the semiconductor and photonics industries suggest many possibilities for achieving sophisticated classes of 3D electronic, optoelectronic, and electromagnetic devices.

REFERENCES AND NOTES

1. V. B. Shenoy, D. H. Gracias, *MRS Bull.* **37**, 847–854 (2012).
2. F. Li, D. P. Josephson, A. Stein, *Angew. Chem. Int. Ed.* **50**, 360–388 (2011).
3. N. B. Crane, O. Onen, J. Carballo, Q. Ni, R. Guldiken, *Microfluid. Nanofluid.* **14**, 383–419 (2013).
4. J. H. Jang et al., *Adv. Funct. Mater.* **17**, 3027–3041 (2007).
5. J. Fischer, M. Wegener, *Laser Photonics Rev.* **7**, 22–44 (2013).
6. K. A. Arpin et al., *Adv. Mater.* **22**, 1084–1101 (2010).
7. W. L. Noorduin, A. Grinthal, L. Mahadevan, J. Aizenberg, *Science* **340**, 832–837 (2013).
8. P. X. Gao et al., *Science* **309**, 1700–1704 (2005).
9. M. Huang, F. Cavallo, F. Liu, M. G. Lagally, *Nanoscale* **3**, 96–120 (2011).
10. M. Tian et al., *Nat. Mater.* **11**, 986–994 (2012).
11. T. G. Leong et al., *Proc. Natl. Acad. Sci. U.S.A.* **106**, 703–708 (2009).
12. M. Yu et al., *ACS Nano* **5**, 2447–2457 (2011).
13. D. Bishop, F. Pardo, C. Bolle, R. Giles, V. Aksyuk, *J. Low Temp. Phys.* **169**, 386–399 (2012).
14. R. J. Wood, *Am. Sci.* **102**, 124–131 (2014).
15. R. Songmuang, A. Rastelli, S. Mendach, O. G. Schmidt, *Appl. Phys. Lett.* **90**, 091905 (2007).
16. J. H. Lee et al., *Adv. Mater.* **26**, 532–569 (2014).
17. M. Schumann, T. Buckmann, N. Gruhler, M. Wegener, W. Pernice, *Light Sci. Appl.* **3**, e175 (2014).
18. X. Zheng et al., *Science* **344**, 1373–1377 (2014).
19. T. A. Schaedler et al., *Science* **334**, 962–965 (2011).
20. C. M. Soukoulis, M. Wegener, *Nat. Photonics* **5**, 523–530 (2011).
21. J. H. Cho et al., *Small* **7**, 1943–1948 (2011).
22. B. Y. Ahn et al., *Science* **323**, 1590–1593 (2009).
23. W. Huang et al., *Nano Lett.* **12**, 6283–6288 (2012).
24. H. Zhang, X. Yu, P. V. Braun, *Nat. Nanotechnol.* **6**, 277–281 (2011).
25. K. Sun et al., *Adv. Mater.* **25**, 4539–4543 (2013).
26. W. Zheng, H. O. Jacobs, *Adv. Funct. Mater.* **15**, 732–738 (2005).
27. X. Guo et al., *Proc. Natl. Acad. Sci. U.S.A.* **106**, 20149–20154 (2009).
28. V. Y. Prinz et al., *Physica E* **6**, 828–831 (2000).
29. O. G. Schmidt, K. Eberl, *Nature* **410**, 168–168 (2001).
30. L. Zhang et al., *Microelectron. Eng.* **83**, 1237–1240 (2006).
31. G. Hwang et al., *Nano Lett.* **9**, 554–561 (2009).
32. W. Gao et al., *Nano Lett.* **14**, 305–310 (2014).
33. See supplementary materials on *Science* Online.
34. D. C. Duffy, J. C. McDonald, O. J. A. Schueller, G. M. Whitesides, *Anal. Chem.* **70**, 4974–4984 (1998).
35. Y. Sun, W. M. Choi, H. Jiang, Y. Y. Huang, J. A. Rogers, *Nat. Nanotechnol.* **1**, 201–207 (2006).
36. D. H. Kim et al., *Science* **333**, 838–843 (2011).
37. S. Yang, K. Khare, P. C. Lin, *Adv. Funct. Mater.* **20**, 2550–2564 (2010).
38. S. Singamaneni, V. V. Tsukruk, *Soft Matter* **6**, 5681–5692 (2010).
39. D. H. Kim, N. S. Lu, Y. G. Huang, J. A. Rogers, *MRS Bull.* **37**, 226–235 (2012).
40. C. P. Yue, S. S. Wong, *IEEE Trans. Electron. Dev.* **47**, 560–568 (2000).

BIOMATERIALS

Electronic dura mater for long-term multimodal neural interfaces

Ivan R. Minev,[1]* Pavel Musienko,[2,3]* Arthur Hirsch,[1] Quentin Barraud,[2] Nikolaus Wenger,[2] Eduardo Martin Moraud,[4] Jérôme Gandar,[2] Marco Capogrosso,[4] Tomislav Milekovic,[2] Léonie Asboth,[2] Rafael Fajardo Torres,[2] Nicolas Vachicouras,[1,2] Qihan Liu,[5] Natalia Pavlova,[2,3] Simone Duis,[2] Alexandre Larmagnac,[6] Janos Vörös,[6] Silvestro Micera,[4,7] Zhigang Suo,[5] Grégoire Courtine,[2]†‡ Stéphanie P. Lacour[1]†‡

The mechanical mismatch between soft neural tissues and stiff neural implants hinders the long-term performance of implantable neuroprostheses. Here, we designed and fabricated soft neural implants with the shape and elasticity of dura mater, the protective membrane of the brain and spinal cord. The electronic dura mater, which we call e-dura, embeds interconnects, electrodes, and chemotrodes that sustain millions of mechanical stretch cycles, electrical stimulation pulses, and chemical injections. These integrated modalities enable multiple neuroprosthetic applications. The soft implants extracted cortical states in freely behaving animals for brain-machine interface and delivered electrochemical spinal neuromodulation that restored locomotion after paralyzing spinal cord injury.

Implantable neuroprostheses are engineered systems designed to study and treat the injured nervous system. Cochlear implants restore hearing in deaf children, deep brain stimulation alleviates Parkinsonian symptoms, and spinal cord neuromodulation attenuates chronic neuropathic pain (1). New methods for recording and modulation of neural activity using electrical, chemical, and/or optical modalities open promising therapeutic perspectives for neuroprosthetic treatments. These advances have triggered the development of myriad neural technologies to design multimodal neural implants (2–5). However, the conversion of these sophisticated technologies into implants mediating long-lasting therapeutic benefits has yet to be achieved. A recurring challenge restricting long-term biointegration is the substantial biomechanical mismatch between implants and neural tissues (6–8).

Neural tissues are viscoelastic (9, 10) with elastic and shear moduli in the 100- to 1500-kPa range. They are mechanically heterogeneous (11, 12) and endure constant body dynamics (13, 14). In contrast, most electrode implants—even thin, plastic interfaces—present high elastic moduli in the gigapascal range, thus are rigid compared to neural tissues (3, 15). Consequently, their surgical insertion triggers both acute and long-term tissue responses (6–8, 14). Here, we tested the hypothesis that neural implants with mechanical properties matching the statics and dynamics of host tissues will display long-term biointegration and functionality within the brain and spinal cord.

We designed and engineered soft neural interfaces that mimic the shape and mechanical behavior of the dura mater (Fig. 1, A and B, and fig. S1). The implant, which we called electronic dura mater or e-dura, integrates a transparent silicone

Science

AAAS

Assembly of micro/nanomaterials into complex, three-dimensional architectures by compressive buckling

Sheng Xu *et al.*

Supplementary Materials for

Assembly of micro/nanomaterials into complex, three-dimensional architectures by compressive buckling

Sheng Xu, Zheng Yan, Kyung-In Jang, Wen Huang, Haoran Fu, Jeonghyun Kim, Zijun Wei, Matthew Flavin, Joselle McCracken, Renhan Wang, Adina Badea, Yuhao Liu, Dongqing Xiao, Guoyan Zhou, Jungwoo Lee, Ha Uk Chung, Huanyu Cheng, Wen Ren, Anthony Banks, Xiuling Li, Ungyu Paik, Ralph G. Nuzzo, Yonggang Huang,* Yihui Zhang,* John A. Rogers*

*Corresponding author. E-mail: jrogers@illinois.edu (J.A.R.); y-huang@northwestern.edu (Y.H.); yihui.zhang2011@gmail.com (Y.Z.)

This PDF file includes:

Materials and Methods

Supplementary Text

Figs. S1 to S23

Materials and Methods

<u>Fabrication methods of three dimensional (3D) mesostructures in silicon, metal, polyimide (PI), photodefinable epoxy (SU8) and combinations of these materials</u>

Preparation of most of the 3D silicon mesostructures began with photolithography and reactive ion etching (RIE) of the top silicon layer on a silicon-on-insulator (SOI) wafer. Immersion in hydrofluoric acid (HF) removed the buried oxide from the exposed regions and also slightly under the edges of the patterned silicon. Spin casting formed a uniform coating (~100 nm) of polytetrafluoroethylene (PTFE) across the substrate and into the undercut regions. Photolithography and wet etching of a thin (50 nm) layer of gold deposited by electron beam evaporation yielded a mask for patterning the PTFE by RIE, in order to selectively expose the bonding sites on silicon. Following removal of the gold, immersion in HF eliminated the remaining buried oxide by complete undercut etching. The PTFE at the edge regions tethered the silicon structures to the underlying wafer. A schematic illustration of the steps is provided in fig. S2. The techniques of transfer printing enabled retrieval of the silicon and delivery to a piece of water soluble tape (polyvinyl alcohol, PVA). A thin (~0.5 mm) sheet of silicone elastomer (Dragon Skin, Smooth-On) served as the assembly platform, stretched to well-defined levels of prestrain (either uniaxial or biaxial, up to levels exceeding ~120%) using a customized stage (fig. S3). Exposing the prestrained elastomer and the two dimensional (2D) silicon precursor (on PVA) to ultraviolet ozone (UVO) yielded hydroxyl termination on their exposed surfaces. Laminating the tape onto the elastomer substrate with the exposed silicon side down, followed by baking in an oven at 70 $^{\mathrm{o}}$C for ~10 min yielded strong covalent bonds between the elastomer substrate and the exposed regions of the silicon. Washing with hot water for ~5 min dissolved away the tape. Drying the sample and then slowly releasing the prestrain completed the 3D assembly process.

Preparation of 3D silicon mesostructures with dimensions in the micron and sub-micron regimes began with deep-UV photolithography to form patterns of poly(methyl methacrylate) (PMMA) on SOI wafers (300 nm and 100 nm thicknesses of silicon for micron and sub-micron cases, respectively). RIE then removed the exposed regions of the top silicon to define the 2D precursors. Following dissolution of the PMMA in acetone, immersion in HF eliminated the buried oxide layer. Transfer printing onto PVA followed by exposure to UVO and execution of process steps similar to those described above completed the assembly.

Preparation of 3D mesostructures in metal began with spin casting a layer of PMMA on a silicon wafer followed by deposition of a layer of SiO_2 (50 nm) by electron beam evaporation. Photolithography and RIE patterned the SiO_2 into geometries that defined the bonding sites. Spin casting formed a uniform overcoat of polyimide (PI; 1.2 μm). The metal consisted of Ni (400~600 nm) deposited by electron beam evaporation onto the PI. Photolithography and etching defined the geometries of 2D precursors in the metal. Spin casting then yielded an additional overcoat of PI (1.2 μm). A thin layer of copper (50 nm) deposited on the PI by electron beam evaporation and patterned by photolithography and wet etching served as a hard mask for oxygen plasma etching of the PI. The residual copper mask was then removed. Immersion in hot acetone partially dissolved the underlying PMMA layer, thereby allowing the entire structure to be retrieved from the silicon wafer and transferred to a stretched elastomer substrate for 3D assembly.

Preparation of 3D mesostructures in PI began with spin casting a layer of PMMA (50 nm) followed by a layer of PI (4 μm) on a silicon wafer. Photolithography and RIE patterned the PI into geometries of the 2D precursors. After removing the PMMA by immersion in acetone, photolithography defined a pattern of photoresist (400 nm) on the PI. Retrieving the structure from the silicon wafer, exposing it to UVO, transferring it to a stretched elastomer substrate and washing away the photoresist configured the system for 3D assembly.

Preparation of 3D mesostructures in a photodefinable epoxy (SU8) began with the deposition of a layer of SiO_2 (500 nm) on a silicon wafer by electron beam evaporation. Spin casting formed a layer of SU8 (4 μm) on top of the SiO_2. Photopatterning the SU8 defined the geometries of the 2D precursors. Immersion in buffered oxide etch (BOE) removed the SiO_2 from the exposed regions and also slightly from under the edges of the SU8. Photolithography created a pattern of photoresist (1.6 μm) on the SU8. BOE eliminated the remaining SiO_2 by complete undercut etching. The remaining steps followed procedures described above.

Preparation of 3D mesostructures that include both Au and SU8 began with deposition of a layer of SiO_2 (500 nm) on a silicon wafer by electron beam evaporation. Photopatterning the SU8 (4 μm) defined the geometries of the 2D precursors. Photolithography and lift-off created patterns of chromium (5 nm) and gold (50 nm) deposited by electron beam evaporation on top of the SU8. Spin-casting and photopatterning formed a thin (500 nm) overcoat of SU8 in a matching geometry. The remaining steps followed procedures described above.

Supplementary Text

1. Finite element analysis (FEA)

Full 3D FEA was adopted to analyze the post-buckling behaviors of 2D precursors (filamentary ribbons made of silicon, metal or polymer) under compressive forces associated with selective bonding to an elastomeric substrate (Dragon Skin; thickness 0.5 mm) that is subsequently released from a state of uniaxial or biaxial prestrain. The elastic modulus (E) and Poisson's ratio (v) are $E_{substrate} = 166$ kPa and $v_{substrate} = 0.49$ for substrate; $E_{Si} = 130$ GPa and $v_{Si} = 0.27$ for Silicon; $E_{Ni} = 200$ GPa and $v_{Ni} = 0.31$ for Nickel; $E_{SU8} = 4.02$ GPa and $v_{SU8} = 0.22$ for SU8; and $E_{PI} = 2.5$ GPa and $v_{PI} = 0.34$ for PI. Eight-node 3D solid elements and four-node shell elements were used for the substrate and filamentary, respectively, and refined meshes were adopted to ensure the accuracy. Linear buckling analyses were carried out to determine the critical buckling strain and lowest buckling mode for the filamentary ribbons, which were then implemented as initial geometric imperfections in the postbuckling simulation. The deformed configurations of various 2D precursors were obtained from FEA under uniaxial or biaxial stretch, as shown in Figs. 1-4, figs. S1, S4, S14, and S16-S19. The agreement between FEA and experiment is remarkably good. The maximum principal strain during the postbucking process can also be calculated; the results are consistent with the analytic model in fig. S6. The average twisting curvature (κ_{twist}) and bending curvature (κ_{bend}) are also calculated from FEA, which can be then used to determine the magnitude of mode ratio (R) for different 3D architectures, based on $R = \kappa_{twist}/\kappa_{bend}$.

2. Analytic model of the geometrical configuration of a 3D helix

A simplified analytic model was developed to describe the geometrical configuration of the central axis of the 3D helix formed from our controlled buckling approach. Consider a

serpentine wire consisting of two arcs, each with the radius of r_0 and top angle of θ_0, as shown in fig. S5A. A Cartesian coordinate system has its origin at the left end of the wire, where the x and z axes correspond to the axial and out-of-plane direction of the serpentine wire. A parametric coordinate θ denotes the location of the central axis of the arcs, such that $\theta \in [0, \ \theta_0]$ and $[\theta_0, \ 2\theta_0]$ represent the first and second arc, respectively. The initial configuration of the central axis can be denoted by the following parametric equation,

$$
\begin{cases}
x_0 = r_0 \left[\sin\dfrac{\theta_0}{2} - \sin\left(\dfrac{\theta_0}{2} - t\right) \right] \\[2mm]
y_0 = r_0 \left[\cos\left(\dfrac{\theta_0}{2} - t\right) - \cos\dfrac{\theta_0}{2} \right] \ , \ 0 \le t \le \theta_0 \text{, and} \\[2mm]
z_0 = 0
\end{cases}
\tag{S1a}
$$

$$
\begin{cases}
x_0 = r_0 \left[3\sin\dfrac{\theta_0}{2} + \sin\left(\dfrac{\theta_0}{2} - t\right) \right] \\[2mm]
y_0 = r_0 \left[\cos\left(\dfrac{\theta_0}{2} - t\right) - \cos\dfrac{\theta_0}{2} \right] \ , \ \theta_0 \le t \le 2\theta_0 . \\[2mm]
z_0 = 0
\end{cases}
\tag{S1b}
$$

In our controlled buckling approach, the two ends of the serpentine wire are bonded to the prestretched substrate. Upon release of the prestrain (ε_{pre}), the ultrathin serpentine wire undergoes compressive strain, $\varepsilon_{compr} = \varepsilon_{pre} / (1 + \varepsilon_{pre})$, leading to its buckling, as shown in fig. S5B. This process can release the relative large strain energy associated with in-plane bending. During this postbuckling process, the displacement (u_2) along y axis is negligible since the compression lies along the x axis and the buckling mainly induces out-of-plane displacements (along the z axis). This expected behavior is consistent with FEA results (fig. S5C), in which the displacement component (u_2) is much smaller than the other two components. FEA results (fig. S5C) also indicate that the displacement component (u_3) can be characterized by a cosine function, $u_3 = br_0 \left[1 - \cos\left(\pi t / \theta_0 \right) \right]$, with the non-dimensional parameter b to be determined. The axial displacement (u_1) consists of two parts, a uniform part ($u_{1uniform} = -\varepsilon_{pre} x_0 (t) / (1 + \varepsilon_{pre})$) due to the global compression from two ends, and a non-uniform part ($u_{1non\text{-}uniform}$) due to the local bending and twisting. FEA results (fig. S5D) indicate that the non-uniform part (u_1) can be described well by a sinusoidal function, $u_{1non\text{-}uniform} = c_1 r_0 \sin\left(\pi t / \theta_0 \right)$, with the parameter c_1 to be determined. FEA calculations also show that c_1 is approximately proportional to the compressive strain, i.e., $c_1 = c_2 (\theta_0) \varepsilon_{compr}$, and is almost independent of the material parameters

4

and cross-sectional geometric parameters (width and thickness). Based on these observations, the deformed configuration of the 3D helix can be written as

$$
\begin{cases}
x = \dfrac{r_0}{1+\varepsilon_{pre}}\left[\sin\dfrac{\theta_0}{2} - \sin\left(\dfrac{\theta_0}{2}-t\right)\right] + \dfrac{c_2(\theta_0)\varepsilon_{pre}r_0}{1+\varepsilon_{pre}}\sin\dfrac{\pi t}{\theta_0} \\[2mm]
y = r_0\left[\cos\left(\dfrac{\theta_0}{2}-t\right)-\cos\dfrac{\theta_0}{2}\right] \\[2mm]
z = br_0\left(1-\cos\dfrac{\pi t}{\theta_0}\right)
\end{cases}
, \; 0 \le t \le \theta_0 , \text{ and} \tag{S2a}
$$

$$
\begin{cases}
x = \dfrac{r_0}{1+\varepsilon_{pre}}\left[3\sin\dfrac{\theta_0}{2} + \sin\left(\dfrac{\theta_0}{2}-t\right)\right] + \dfrac{c_2(\theta_0)\varepsilon_{pre}r_0}{1+\varepsilon_{pre}}\sin\dfrac{\pi t}{\theta_0} \\[2mm]
y = r_0\left[\cos\left(\dfrac{\theta_0}{2}-t\right)-\cos\dfrac{\theta_0}{2}\right] \\[2mm]
z = br_0\left(1-\cos\dfrac{\pi t}{\theta_0}\right)
\end{cases}
, \; \theta_0 \le t \le 2\theta_0 . \tag{S2b}
$$

The pitch of the 3D helix is $4r_0\sin(\theta_0/2)/(1+\varepsilon_{pre})$. Because the wire is highly flexible, its membrane strain can be neglected, such that the total arc length along the central axis will remain unchanged during the postbuckling. The associated requirement can be written as

$$
2\int_0^{\theta_0}\sqrt{(dx/dt)^2 + (dy/dt)^2 + (dz/dt)^2}\,dt = 2\theta_0 r_0 , \tag{S3a}
$$

which can be re-arranged to

$$
\int_0^{\theta_0}\sqrt{\left[\dfrac{\cos\left(t-\dfrac{\theta_0}{2}\right)}{1+\varepsilon_{pre}} + \dfrac{c_2(\theta_0)\varepsilon_{pre}}{1+\varepsilon_{pre}}\dfrac{\pi}{\theta_0}\cos\dfrac{\pi t}{\theta_0}\right]^2 + \sin^2\left(t-\dfrac{\theta_0}{2}\right) + b^2\left(\dfrac{\pi}{\theta_0}\right)^2\sin^2\dfrac{\pi t}{\theta_0}}\,dt = \theta_0 . \tag{S3b}
$$

Solving Eq. (S3b) defines the non-dimensional parameter b for a given ε_{pre} and θ_0, noting that c_2 is calculated by FEA. For $\theta_0 = 3\pi/4$ and $\varepsilon_{pre} = 90\%$ used in the experiment of straight helix (Fig. 1B and fig. S4), the parameters are $b = 0.85$ and $c_2 = 0.35$.   The corresponding configurations of the 3D helix derived using this analytic model appear in fig. S4. The results agree well between experiment and FEA. Note that straight wires were between each unit cell in fig. S4 to capture the effects of the bonding sites adopted in experiment.

5

3. Analytic model for the maximum strain in a 3D silicon helix during postbuckling

We analyze the effects of geometric parameters on the maximum strain in the 3D silicon helix, and determine a scaling law for the maximum thickness to avoid fracture of the structure. The twisting and out-of-plane bending strains during the postbuckling process are proportional to the thickness, while the in-plane bending strain is proportional to the width. Assuming elastic behavior, the maximum principal strain in the postbuckling regime can be expressed as

$$\varepsilon_{\max} = F_1\left(\varepsilon_{compr}, \theta_0\right)\frac{t}{r_0} + F_2\left(\varepsilon_{compr}, \theta_0\right)\frac{w}{r_0}, \tag{S4}$$

where F_1 and F_2 are non-dimensional functions of the compressive strain (ε_{compr}) associated with prestrain in the substrate, and the top angle (θ_0) of arcs in the serpentine wire. The strain component induced by out-of-plane bending and twisting is linearly proportional to the square root of the compressive strain during postbuckling, i.e., $F_1 \sim \sqrt{\varepsilon_{compr}}$. This relation is confirmed by FEA results in fig. S6A. The numerical results in fig. S6B also show that the function F_2 is linearly proportional to the compressive strain, ε_{compr}, such that Eq. (S4) can be written as

$$\varepsilon_{\max} = g_1\left(\theta_0\right)\sqrt{\varepsilon_{compr}}\,\frac{t}{r_0} + g_2\left(\theta_0\right)\varepsilon_{compr}\,\frac{w}{r_0}, \tag{S5}$$

where g_1 and g_2 are the coefficients of proportionality between F_1 and $\sqrt{\varepsilon_{compr}}$ and between F_2 and ε_{compr}, respectively, and both depend on the top angle (θ_0) of arcs in the serpentine wire. For $\theta_0 = 3\pi/4$ used in the experiment, g_1 and g_2 can be calculated as 1.47 and 8.82×10^{-3}, based on FEA. With Eq. (S5) and a fracture criterion of $\varepsilon_{max} = \varepsilon_{fracture}$, where $\varepsilon_{fracture}$ is the fracture strain of the serpentine material (e.g., ~2% for silicon), the maximum dimensionless thickness that can be achieved without fracture can be written as

$$\frac{t_{\max}}{r_0} = \frac{\varepsilon_{fracture}}{g_1\left(\theta_0\right)}\sqrt{\frac{1+\varepsilon_{pre}}{\varepsilon_{pre}}} - \frac{g_2\left(\theta_0\right)}{g_1\left(\theta_0\right)}\frac{w}{r_0}\sqrt{\frac{\varepsilon_{pre}}{1+\varepsilon_{pre}}}, \tag{S6}$$

where the relation between prestrain of substrate and the corresponding compressive strain of serpentine wire is adopted, i.e., $\varepsilon_{compr} = \varepsilon_{pre}/\left(1+\varepsilon_{pre}\right)$. For a target prestrain level of 100%, the maximum dimensionless thickness ($t_{\max}/r_0$) can be calculated based on Eq. (S6), as shown in fig. S6C. The values decrease slightly with increasing dimensionless width (w/r_0), in a linear manner, which agrees with the corresponding FEA results. This result is also consistent with experiment measurements on two different precursor designs, in which the design with $t/r_0 = 0.0063$ and $w/r_0 = 0.29$ survives the postbuckling process, and the design with $t/r_0 = 0.032$ and $w/r_0 = 0.29$ fractures. Based on the analytic model (Eq. (S6)), we can also obtain the maximum thickness for different levels of prestrain, as shown in fig. S6D. For a typical dimensionless width of $w/r_0 = 0.2$, the maximum allowable thickness ($t_{\max}$) reduces from ~$0.027r_0$ to ~$0.015r_0$, if the target prestrain of substrate increases from 50% to 200%.

4. Energetic analysis to estimate the lower bound for the work of adhesion at the bonding regions

The bonding regions may delaminate for a thick 2D precursor under a large level of prestrain, or for a precursor with small bonding pads. From the energetic point of view, the failure mode of delamination only occurs if the total potential energy U_{total} for the un-delaminated state (i.e., the state of successfully pop-up 3D configuration) is larger than its counterpart, zero, for the delaminated state. Here U_{total} can be expressed as $U_{total} = W_{strain} - A_{bonding}\gamma_{bonding}$, where W_{strain} is the strain energy in the successfully pop-up configuration; the second term corresponds to the adhesion energy, with $\gamma_{bonding}$ representing the work of adhesion at the bonding region, and $A_{bonding}$ the area of bonding pads. For those 3D mesostructures that form successfully in experiment, the corresponding total potential energy U_{total} should be smaller than zero, which leads to $\gamma_{bonding} \geq W_{strain}/A_{bonding}$. Combined with FEA for the calculations of strain energy, this equation could give an approximate estimation on the lower bound of $\gamma_{bonding}$. Five representative 3D mesostructures are analyzed, including the helices with three different widths (in Fig. 1, B and E, and fig. S4), the two-layer flower (in Fig. 2C) and the peacock (in Fig. 3A), which suggest the work of adhesion ($\gamma_{bonding}$) to be greater than ~8.2 J/m^2. This magnitude is comparable to the strong adhesion (~20.6 J/m^2 or 10.1 J/m^2) between graphene and SiO$_x$/Si substrates after using vacuum annealing or rapid thermal annealing to form C$-$O and C=O chemical bonds at the interface, or the adhesion energy (~7.0 J/m^2) between silicon nitride and organosilicate glass films after using UV irradiation to form SiO$-$N bonds at the interface during the deposition process of silicon nitride, or the adhesion energy (~3.0 J/m^2) at the interface of two bonded PMMA chips after using UVO treatment to improve the bonding.

5. Cage inductor radiofrequency (RF) measurement de-embedding algorithm

The RF measurements used test fixtures as in fig. S20. The resistances of all of the devices are around ~47 Ω. The resistance, together with the elastomer substrate thickness and permittivity are all taken into consideration during the electromagnetic modeling. Parasitic effects introduced by feedlines must be removed to obtain the real performance of the device under test (DUT). An open-through de-embedding technique calibrates out the feedline effects (23). A lumped equivalent circuit model captures the physics of parasitic effects. Feedlines are designed as short as possible to minimize the distribution effect. Open-through de-embedding patterns are shown in fig. S20. As in fig. S20A, an admittance Π-network was used to model the capacitive effects between the contact pads and the surrounding environment including the substrate and RF ground. Series connected impedance network was used to model the resistance and inductance of the feedlines. The schematic views of patterns with the DUT, without the DUT (open case) and shorted case are shown in figs. S20A, 20B and 20C, respectively. Corresponding lumped equivalent circuits were constructed to model the RF performance of each pattern.

The mathematical procedure for open-through de-embedding is shown in fig. S21. The first step is shown in fig. S21A, which abstracts the admittance Π-network (open pattern) from the original data. The result still contains the parasitic resistances and inductances (Z1 and Z2) whose total effect can be calculated according to step 2 shown in fig. S21B. Finally, the real performance of DUT can be obtained through step 3.

6. Measured raw data of samples with 54%, 33% and 0% substrate prestrain

The measured raw data are shown in fig. S22 for samples with (A) 54%, (B) 33%, and (C) 0% substrate prestrain in the form of Smith Charts from 10 MHz to 10 GHz using an Agilent N5230A PNA-L Network Analyzer capable of measurement from 10 MHz - 40 GHz.

7. Derivation of effective inductance, Q factor and self-resonance frequency of cage inductors

The lumped equivalent circuit of cage inductor is shown in fig. S23. Its admittance matrix of the network is derived as

$$Y = \begin{bmatrix} Y_p + Y_s & -Y_s \\ -Y_s & Y_p + Y_s \end{bmatrix},$$
(S7)

Matrix Y can be obtained from the feed lines decoupled high frequency structural simulator (HFSS) simulated or measured S parameters. The total effective inductance L_{etotal} and Q factor Q_{total} can be then derived from the matrix Y as shown in (S8) and (S9):

$$L_{etotal} = \frac{\mathrm{Im}\left(-\dfrac{1}{Y_{12}}\right)}{\omega},$$
(S8)

$$Q_{total} = -\frac{\mathrm{Im}(Y_{11})}{\mathrm{Re}(Y_{11})}.$$
(S9)

Self-resonance frequency f_0 is then derived when $Q_{total}=0$.

A. 3D view I

Experiment

FEA

ε_{max}
0.0   0.9%
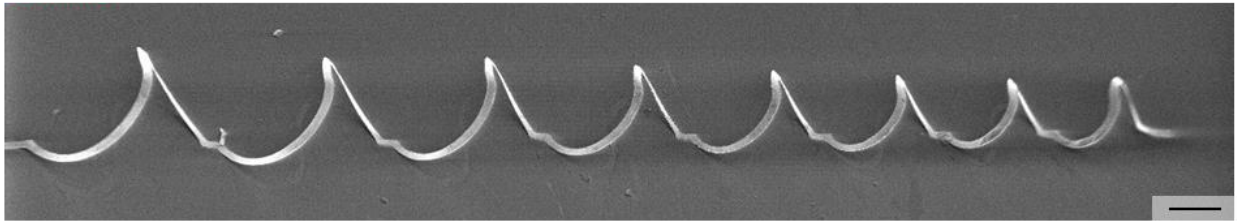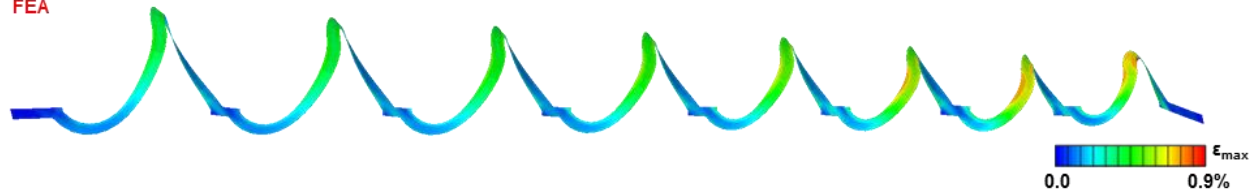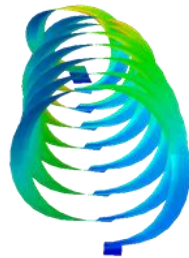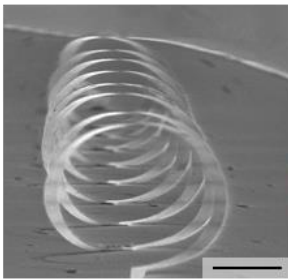
B. 3D view II

C. 3D view III
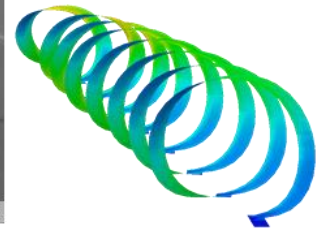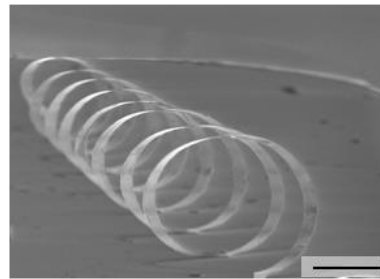
Fig. S1.

Experimental images and corresponding FEA predictions for a 3D conical helix based on silicon ribbons, viewed at three different angles. The color in the FEA results represents the maximum principal strain. The scale bars in all images are 200 μm.
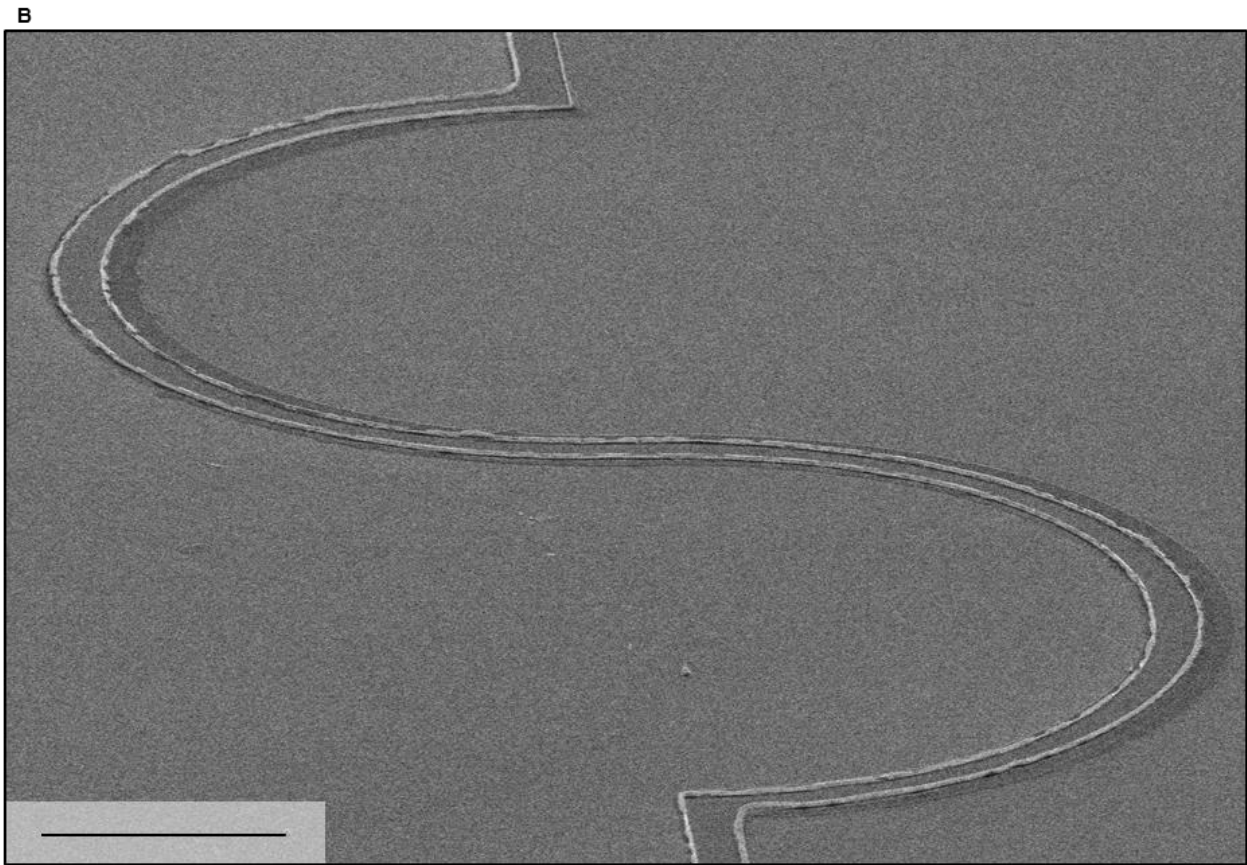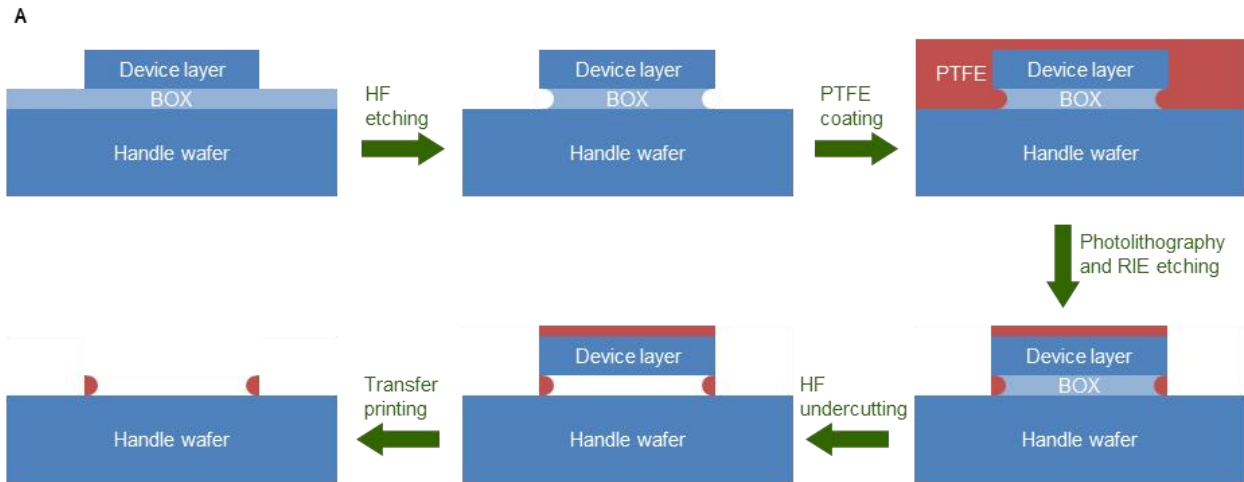
Fig. S2

Typical Fabrication procedure for the 3D structures. (**A**) Schematic fabrication flow chart for the Si structures from SOI wafer, to illustrate the PTFE anchors from undercutting the buried oxide (BOX) layer. (**B**) SEM image of the PTFE anchors after transfer printing the Si membranes. The scale bar in (B) is 100 μm.
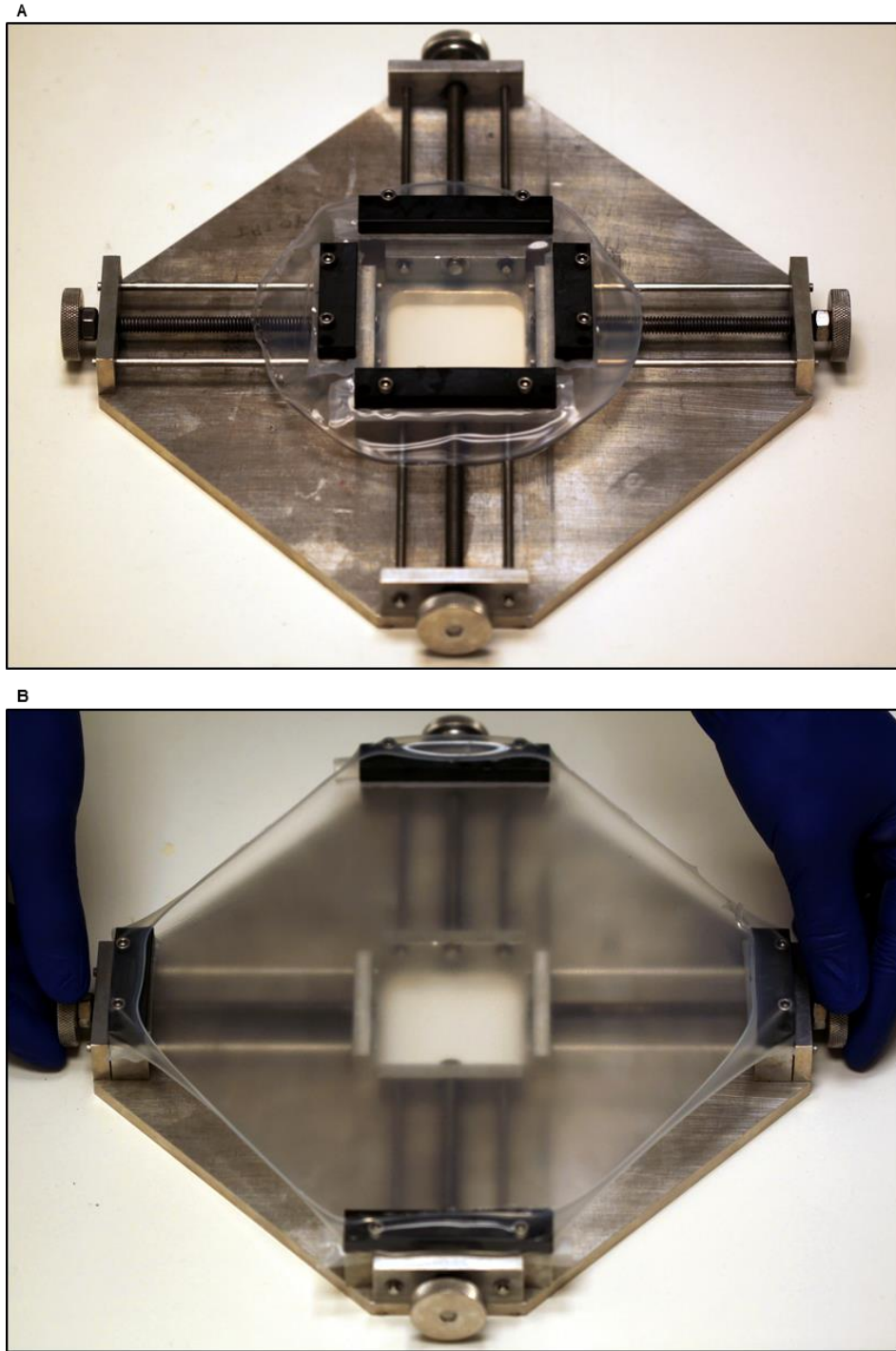
Fig. S3

Optical images of a customized equal-biaxial stretching stage with an elastomer assembly platform. (**A**) Before and (**B**) after prestraining the elastomer substrate to 120%. Here, Dragon Skin (Smooth-On Inc.) is used as the elastomer substrate.
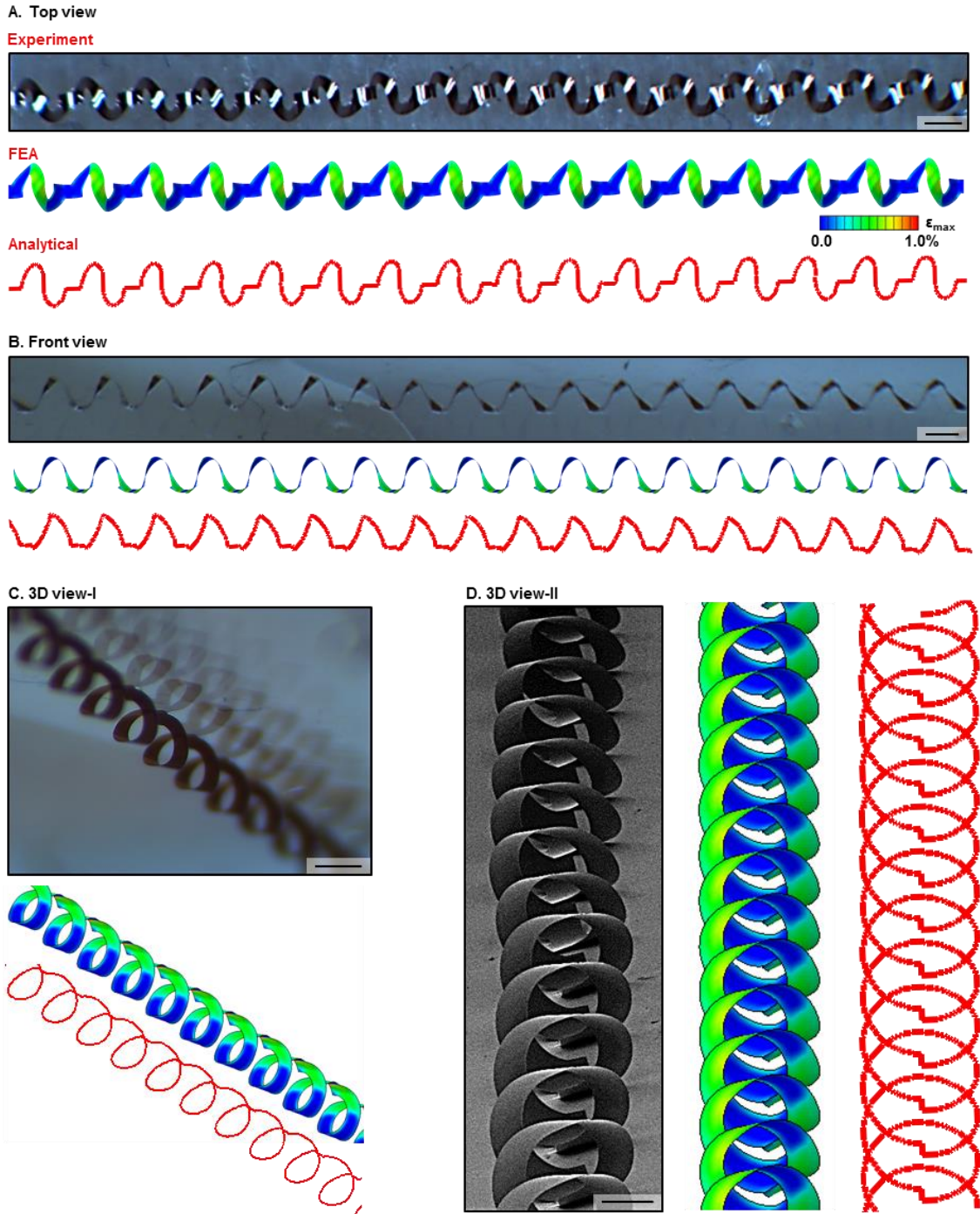
Fig. S4

Experimental images, FEA predictions and corresponding analytic results for a straight helix based on silicon ribbons, viewed at different angles: (**A**) top view, (**B**) front view, (**C**) and (**D**) 3D views. The experimental images in (A), (B) and (C) are optical images; (D) is a SEM image. The color in the FEA results represents the maximum principal strain. The scale bars in (A), (B) and (C) is 500 μm, and that in (D) is 200 μm.
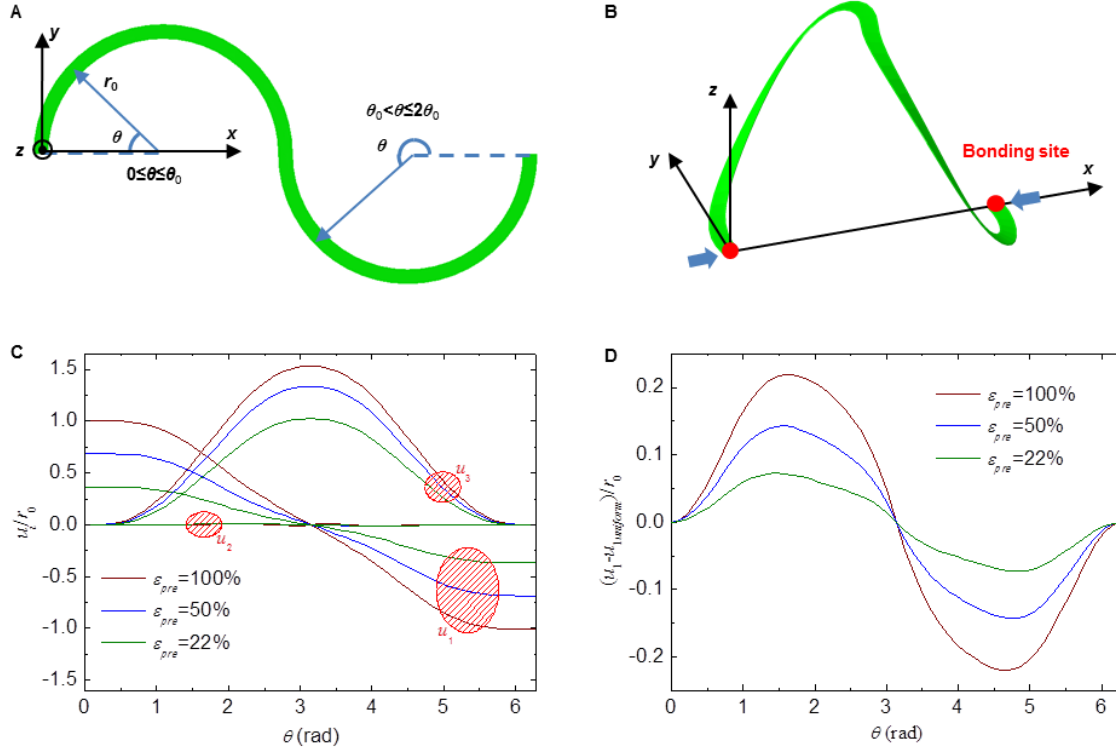
Fig. S5

Schematic illustration and FEA results for the theoretical model of geometric configurations of a 3D helix: (**A**) top view of a serpentine wire consisting of two arcs. (**B**) 3D view of the deformed configuration after compression from the two ends. (**C**) FEA results of the displacement components as a function of the parametric coordinate θ for three different levels of substrate prestrain. (**D**) FEA results of the non-uniform part of the displacement component along the x axis, as a function of the parametric coordinate θ for three different levels of substrate prestrain. The geometric parameters adopted in the FEA are $t = 2.0$ μm, $w = 60$ μm, $r_0 = 500$ μm, and $\theta_0 = 180^\circ$.
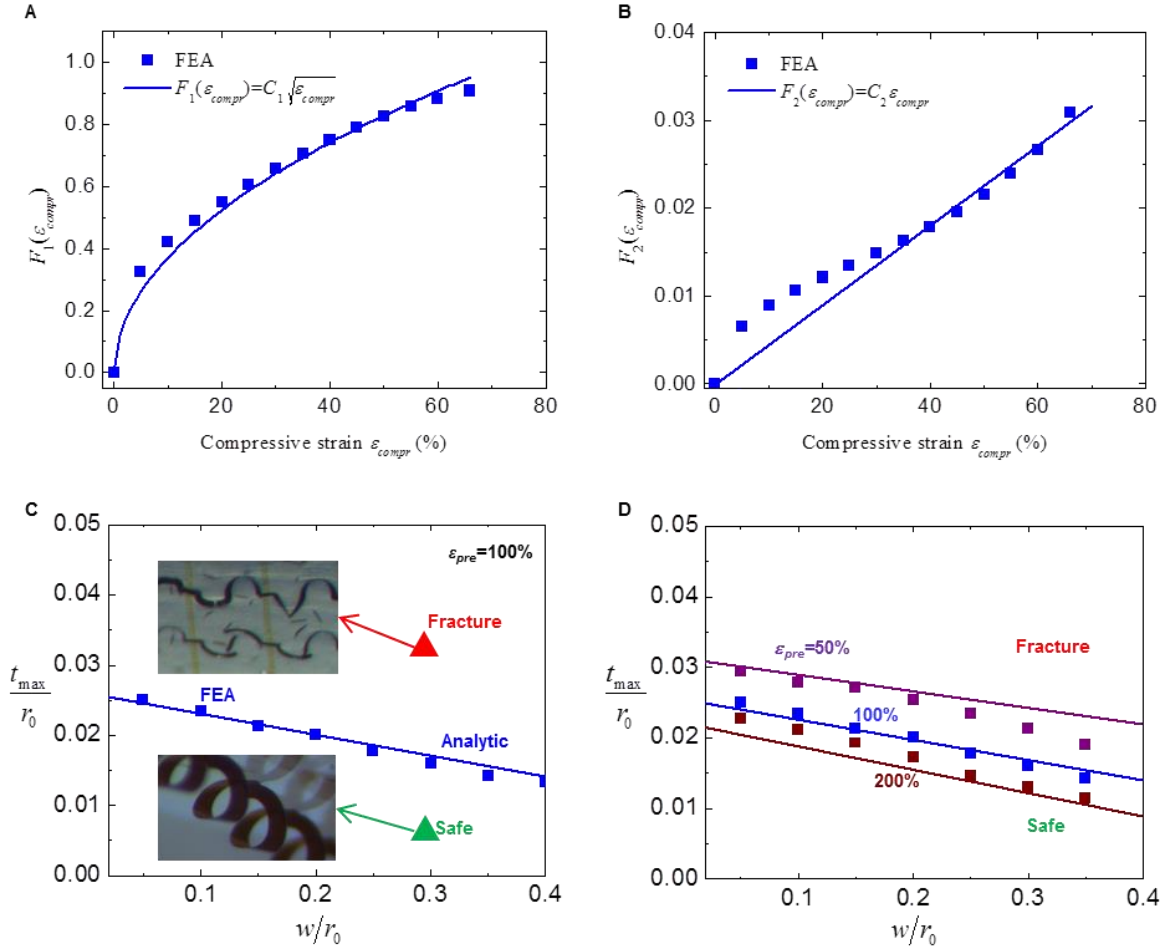
Fig. S6

Scaling law for the maximum principal strain in a 3D helix during the post-buckling process and a design criterion to avoid fracture. Dependence of the functions $F_1(\varepsilon_{compr})$ (**A**) and $F_2(\varepsilon_{compr})$ (**B**) on applied compressive strain. The coefficient $F_1(\varepsilon_{compr})$ of the dominant strain component (due to out-of-plane bending and twisting) is proportional to the square root of the applied strain. The coefficient $F_2(\varepsilon_{compr})$ of the minor strain component (due to in-plane bending) is approximately proportional to the applied strain. (**C**) Maximum dimensionless thickness as a function of the dimensionless width for 100% prestrain, in which the green and red triangles correspond to 3D helices that are observed to remain intact and fracture, respectively, in experiments. (**D**) Fracture map constructed by the analytic model for different levels of prestrain.
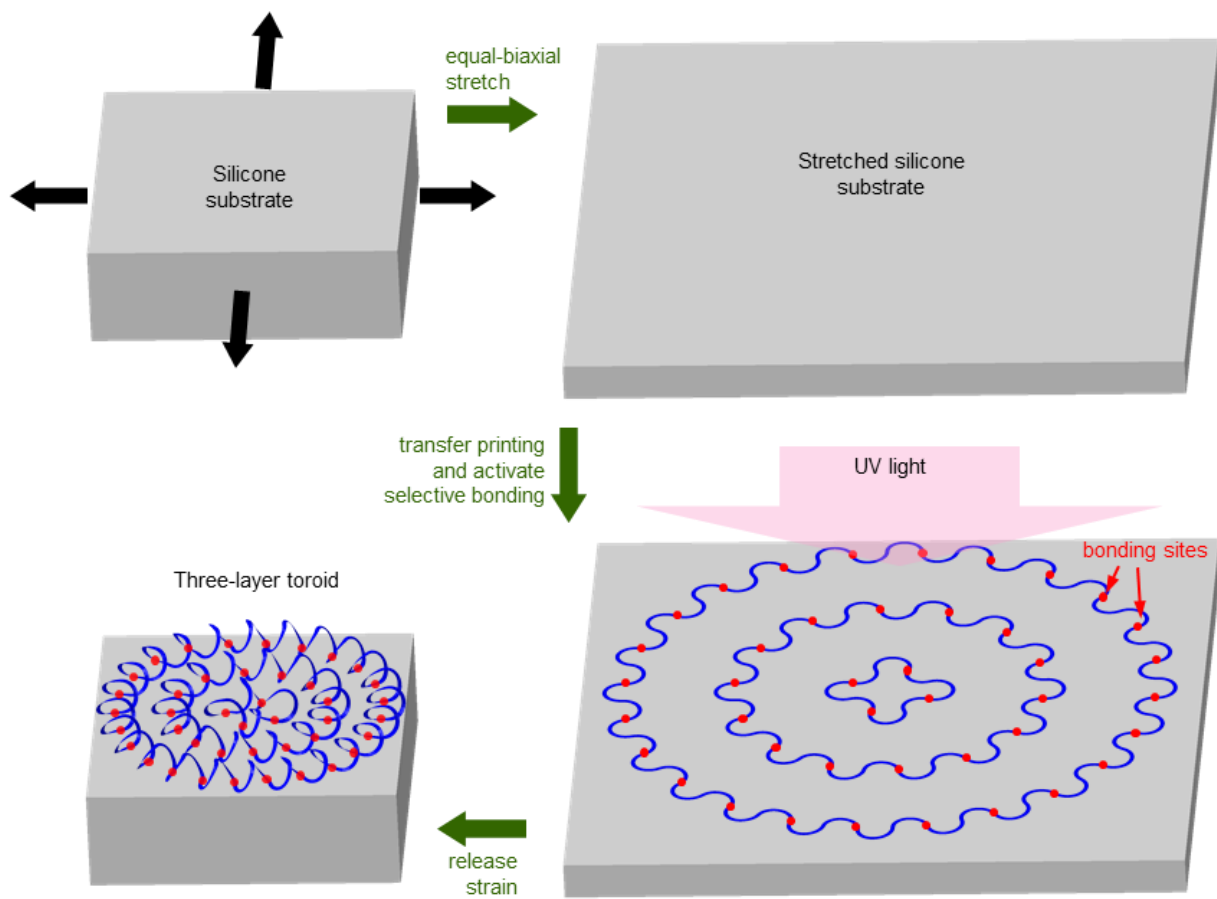
Fig. S7

Schematic illustration of the process for generating 3D structures by using biaxial prestrain in an elastomeric substrate.
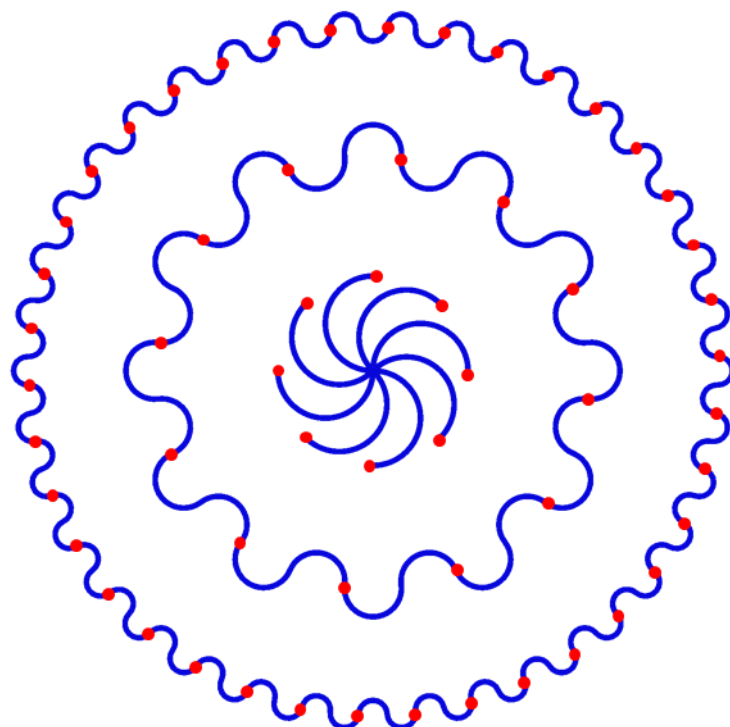
Fig. S8

2D precursor of the three-layer structure shown in Fig. 1G, where the bonding sites are represented by red dots.
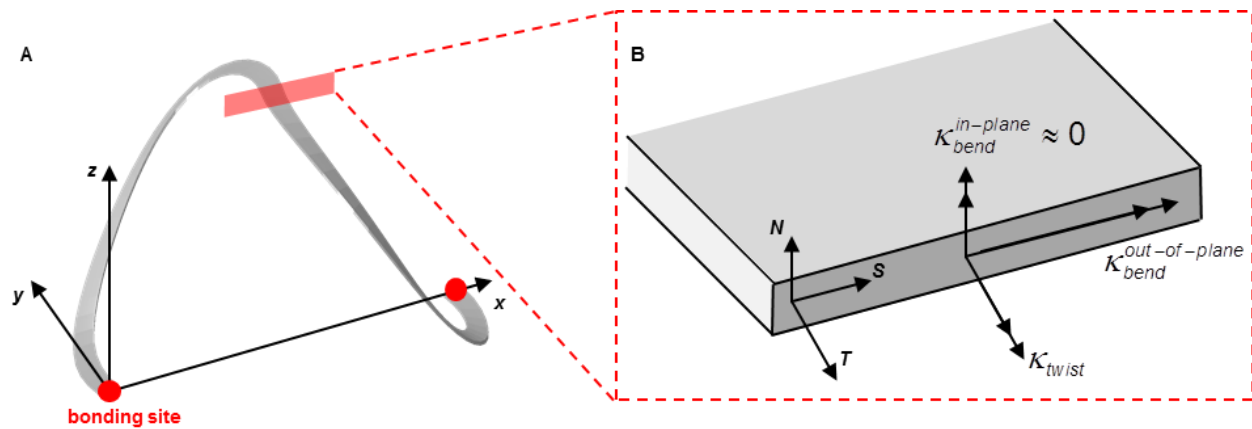
Fig. S9

Schematic illustration of the local coordinate system for a representative 3D structure (i.e., straight helix). (**A**) 3D helix in a global coordinate system (x,y,z). (**B**) Local coordinate system (N,T,S), where N denotes the normal direction, T denotes the tangential direction, and S denotes another principal direction. Consistent with the right-hand rule, the in-plane bending, out-of-plane bending and twisting are along the axes of N, S and T, respectively. Because of the ultrathin nature of the filamentary ribbon, in-plane bending is energetically unfavorable. As a result, the induced change in curvature is negligible, as compared to that associated with twisting or out-of-plane bending.
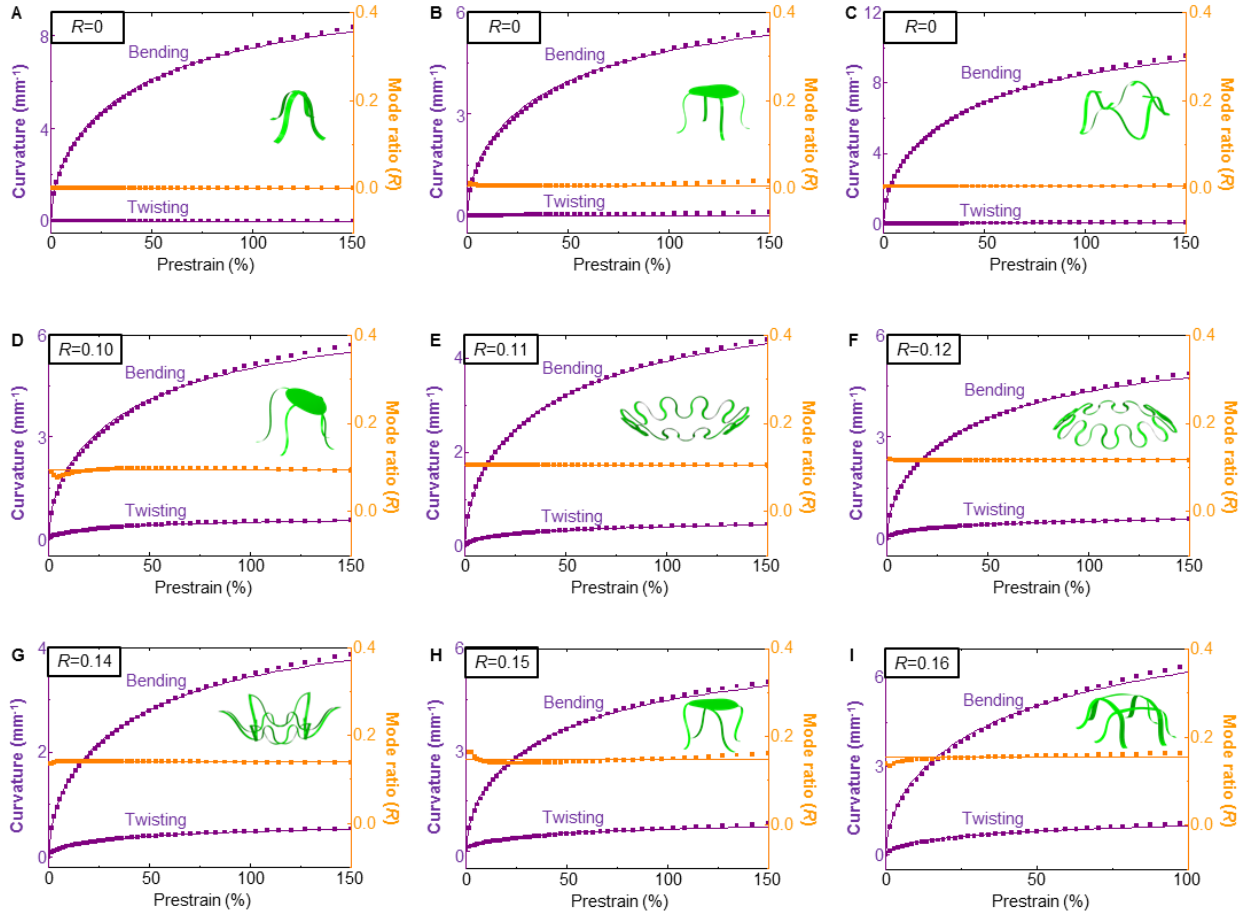
Fig. S10

Curvature components due to bending and twisting as a function of prestrain, for various 3D pop-up structures that have a bending dominated buckling mode: (**A**) tent; (**B**) regular table; (**C**) box I; (**D**) tilted table; (**E**) flower; (**F**) inverted flower; (**G**) two-layer flower; (**H**) rotated table; and (**I**) boxed II.

18
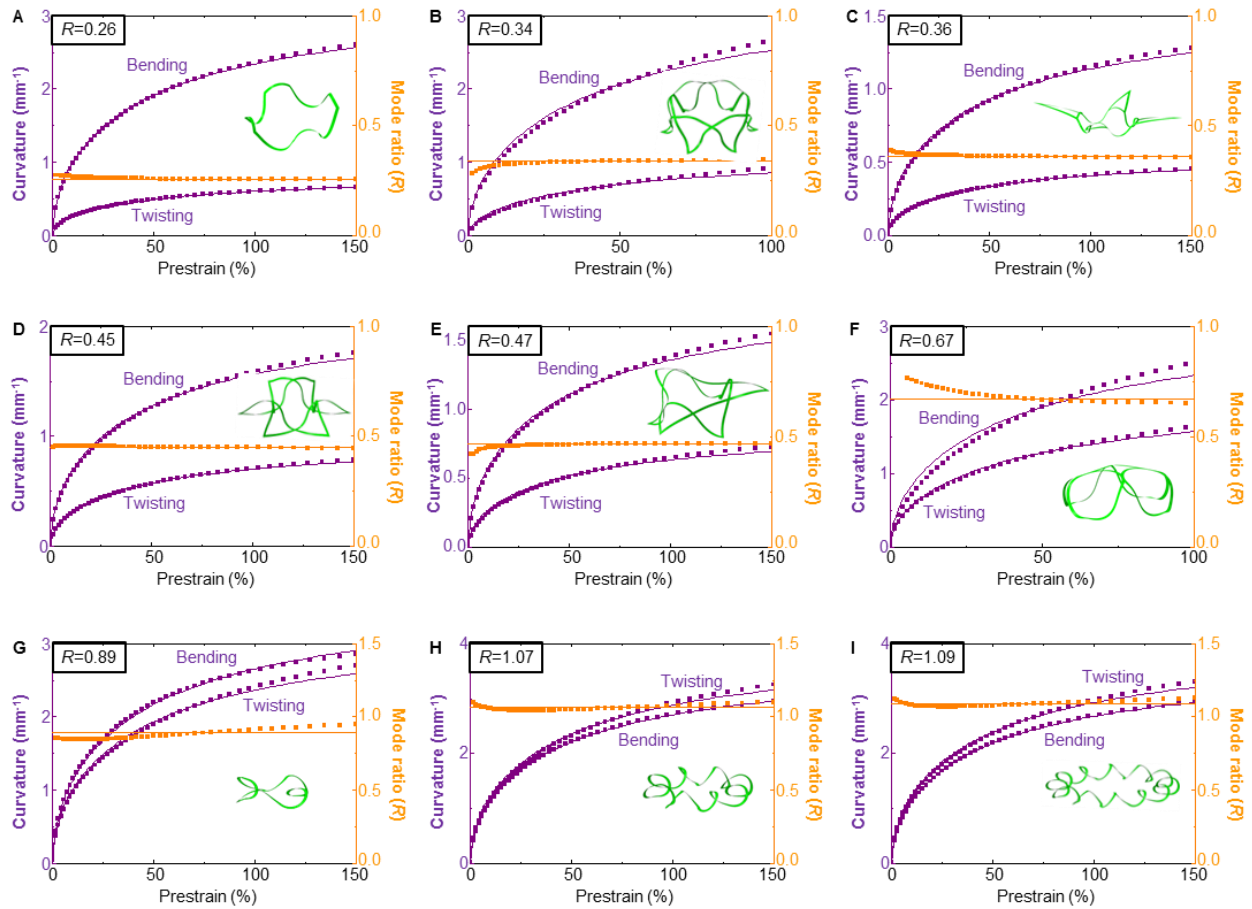
Fig. S11

Curvature components due to bending and twisting as a function of prestrain, for various 3D pop-up structures that have a bending-twisting mixed buckling mode: (**A**) folded box; (**B**) basket; (**C**) star; (**D**) butterfly; (**E**) starfish; (**F**) box with roof; (**G**) circular helix with 4 cells; (**H**) circular helix with 8 cells; and (**I**) circular helix with 12 cells.
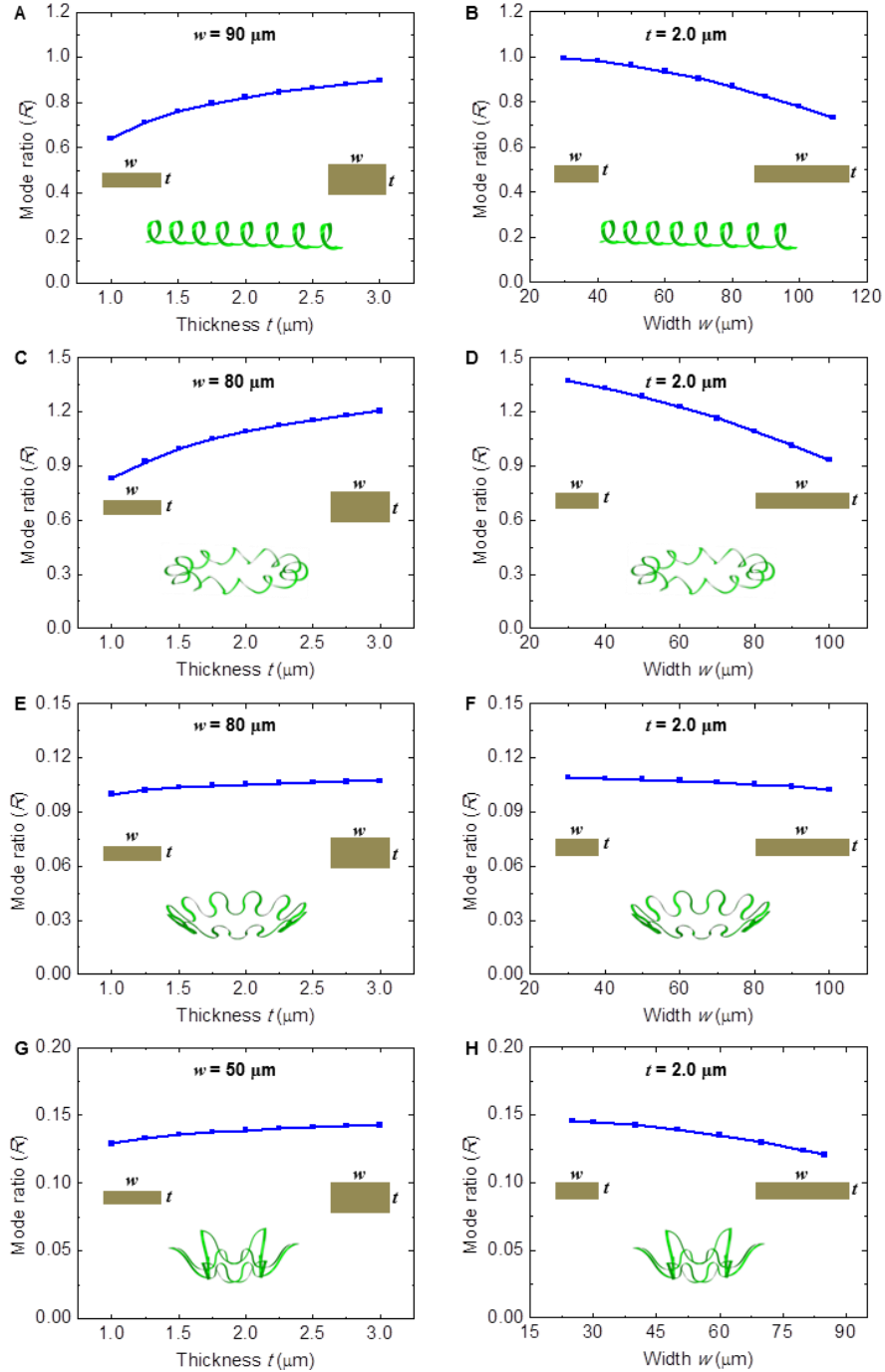
Fig. S12

Effect of cross-sectional geometry on the mode ratio. Mode ratio as a function of thickness and width for (**A**,**B**) a straight helix, (**C**,**D**) a circular helix, (**E**,**F**) a flower, and (**G**,**H**) a two-layer flower. For a bending dominated mode (E-H), the mode ratio is insensitive to changes in the cross-sectional parameters. For a bending-twisting mixed mode (A-D), the mode ratio changes significantly when the thickness (or width) is changed by ~3 times, but is not sufficiently large to induce a mode transition (i.e. from bending-twisting mixed mode to bending dominated mode).
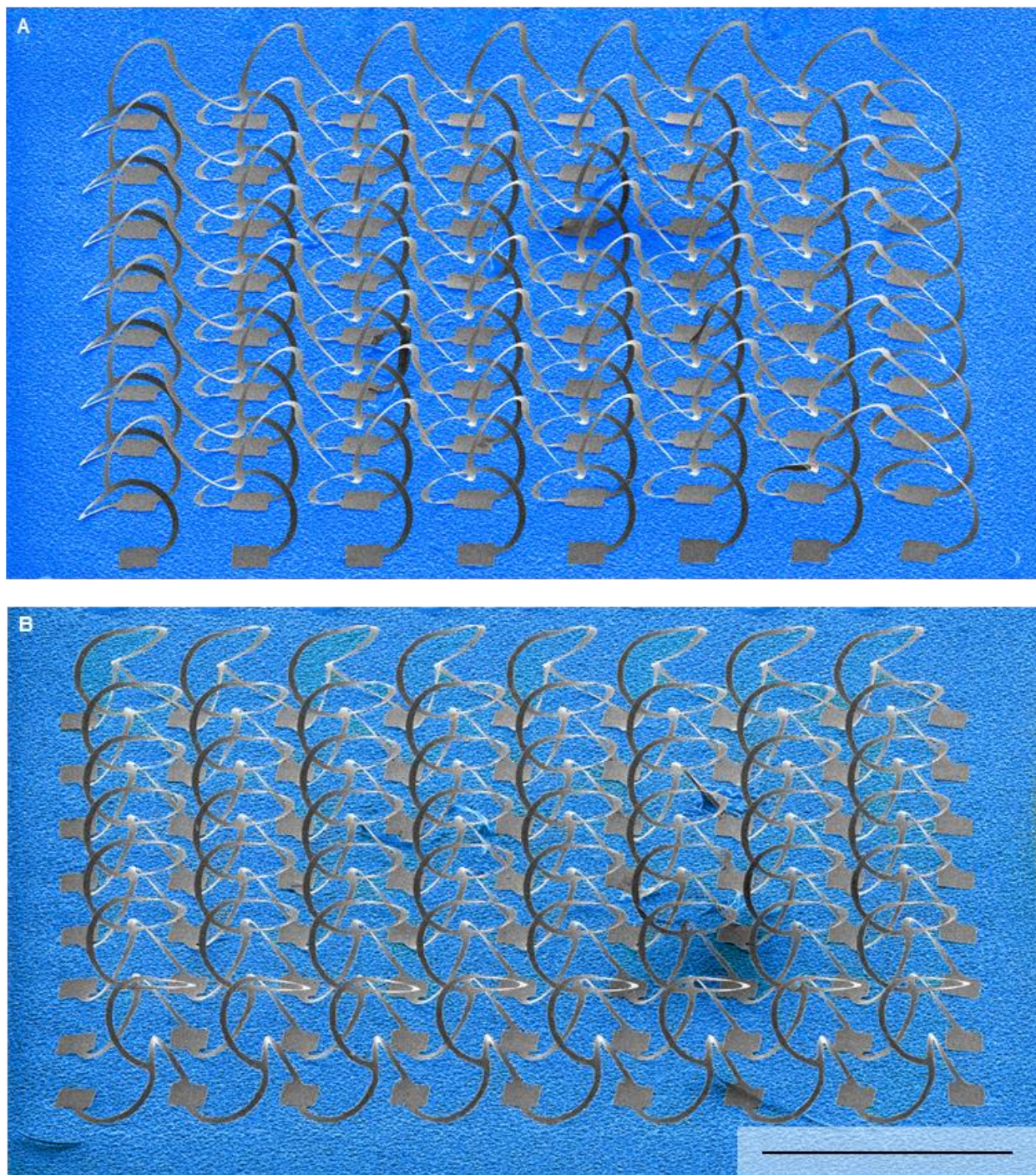
Fig. S13

SEM images with artificial color from orthogonal viewing angles of the 8×8 array of the double-floor helix structure. SEM image showing (**A**) 8 evenly spaced helices on the 1st floor, and (**B**) another 8 evenly spaced helices on the 2nd floor. The scale bar is 1 mm.
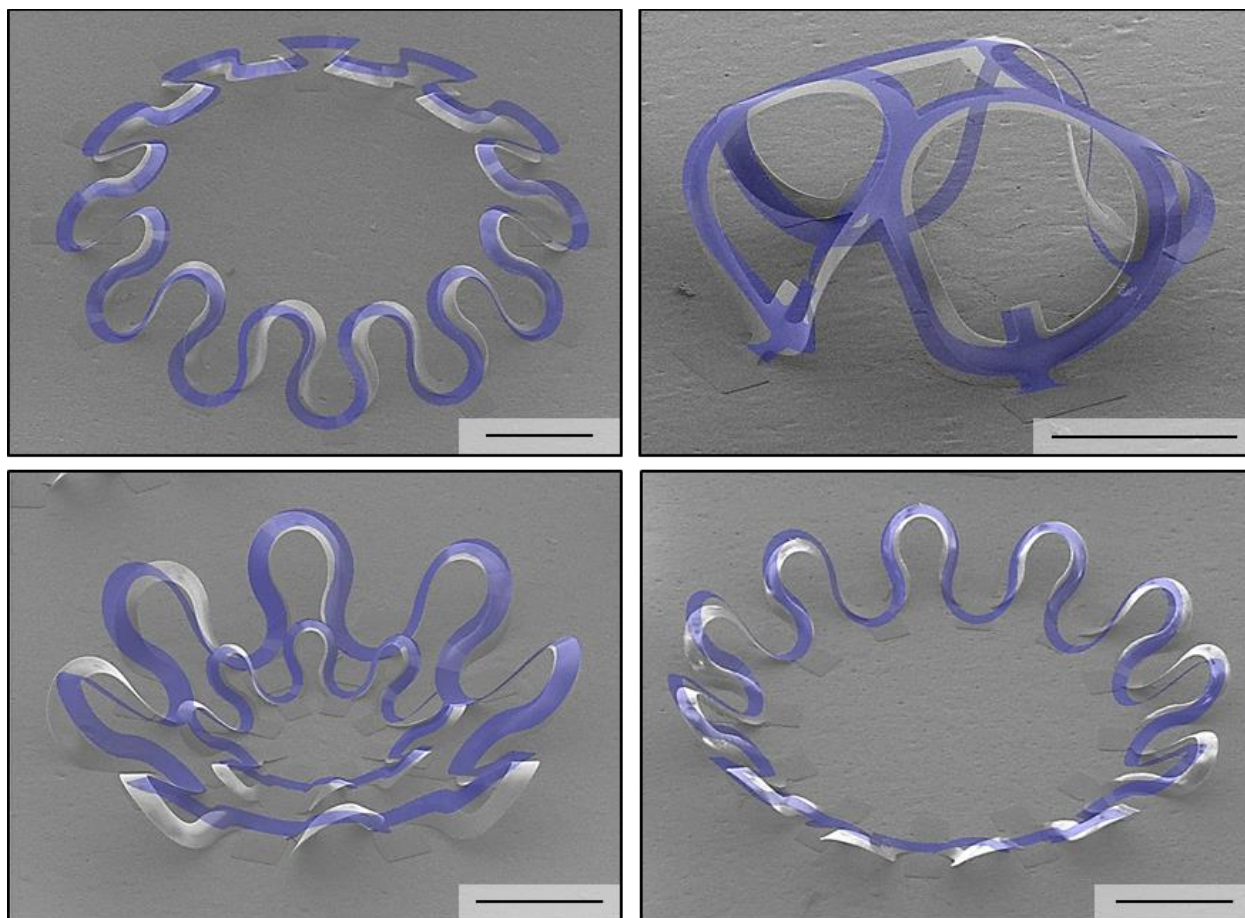
Fig. S14

Various 3D pop-up structures and their corresponding FEA results that do not appear in Figs. 2 or 3. (**A**) Basic 3D ring structure, and three 3D structures (raised ring, inverted flower II, inverted flower III, scaffold, double-floor building, and coil on gallery) generated by hierarchical buckling. (**B**) Advanced assembly of two different types of 3D structures. The scale bars in all images are 200 μm.
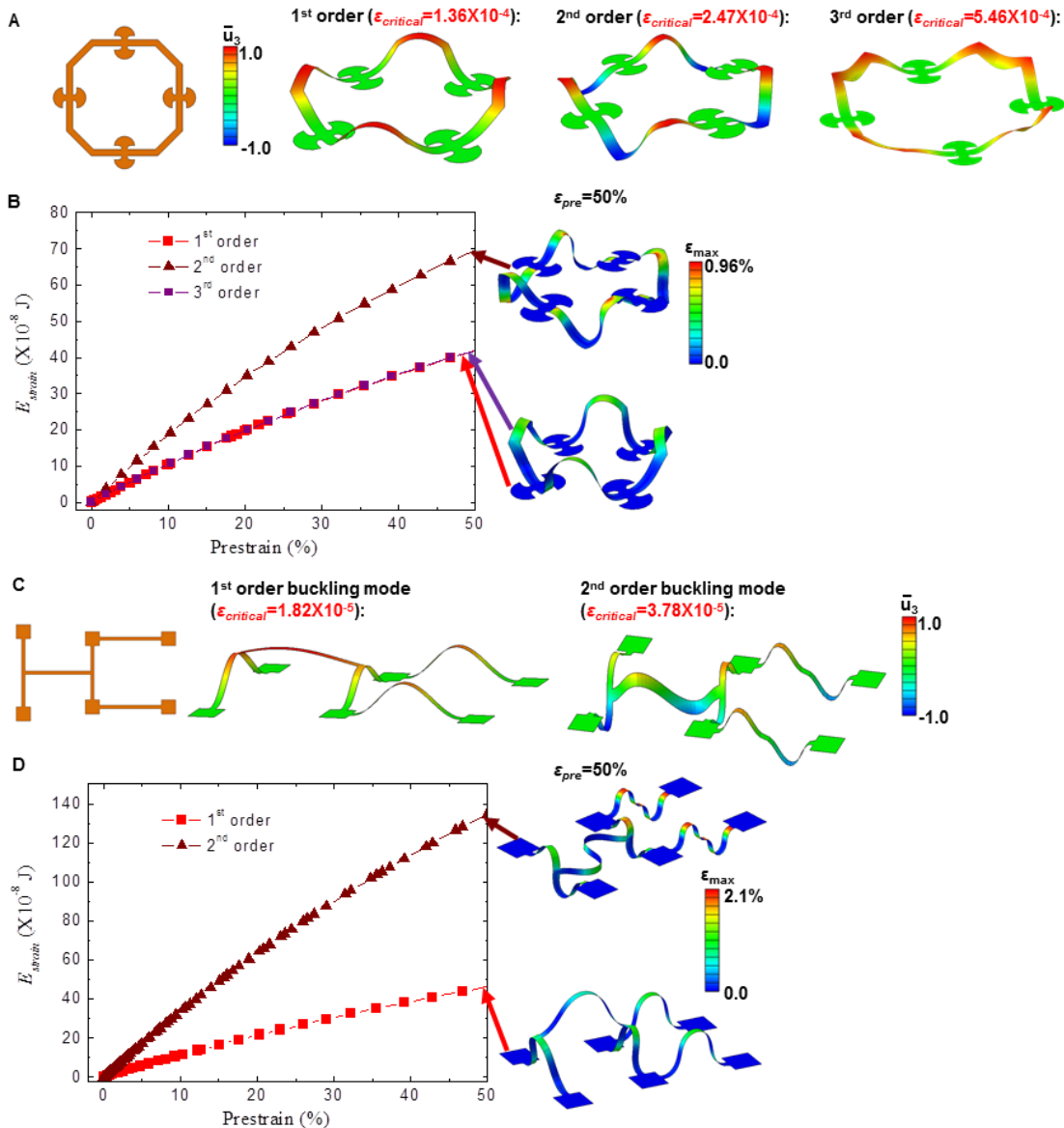
Fig. S15

Uniqueness of the 3D structures. (**A**) 2D precursor of a folded box and its lowest 3 orders buckling modes, where the critical buckling strains (of substrate prestretch) are 0.014%, 0.025% and 0.055%. (**B**) Strain energy as a function of prestrain for the lowest 3 orders buckling modes, in which the 3rd order mode cannot stabilize and therefore transforms rapidly into the 1st order mode as the compression proceeds. (**C**) 2D precursor of the two-floor building and its lowest 2 orders buckling modes, where the critical buckling strains (of substrate prestretch) are 0.0018% and 0.0038%. (**D**) Strain energy as a function of prestrain for the lowest 2 orders buckling modes. The color in (A) and (C) denotes the normalized out-of-plane displacement, and that in (B) and (D) denotes the maximum principal strain. The 1st order mode always corresponds to the lowest strain energy. Therefore, in the absence of defects that coincide with the 2nd order mode, the 1st order mode will be the unique solution. This is consistent with experimental observations.
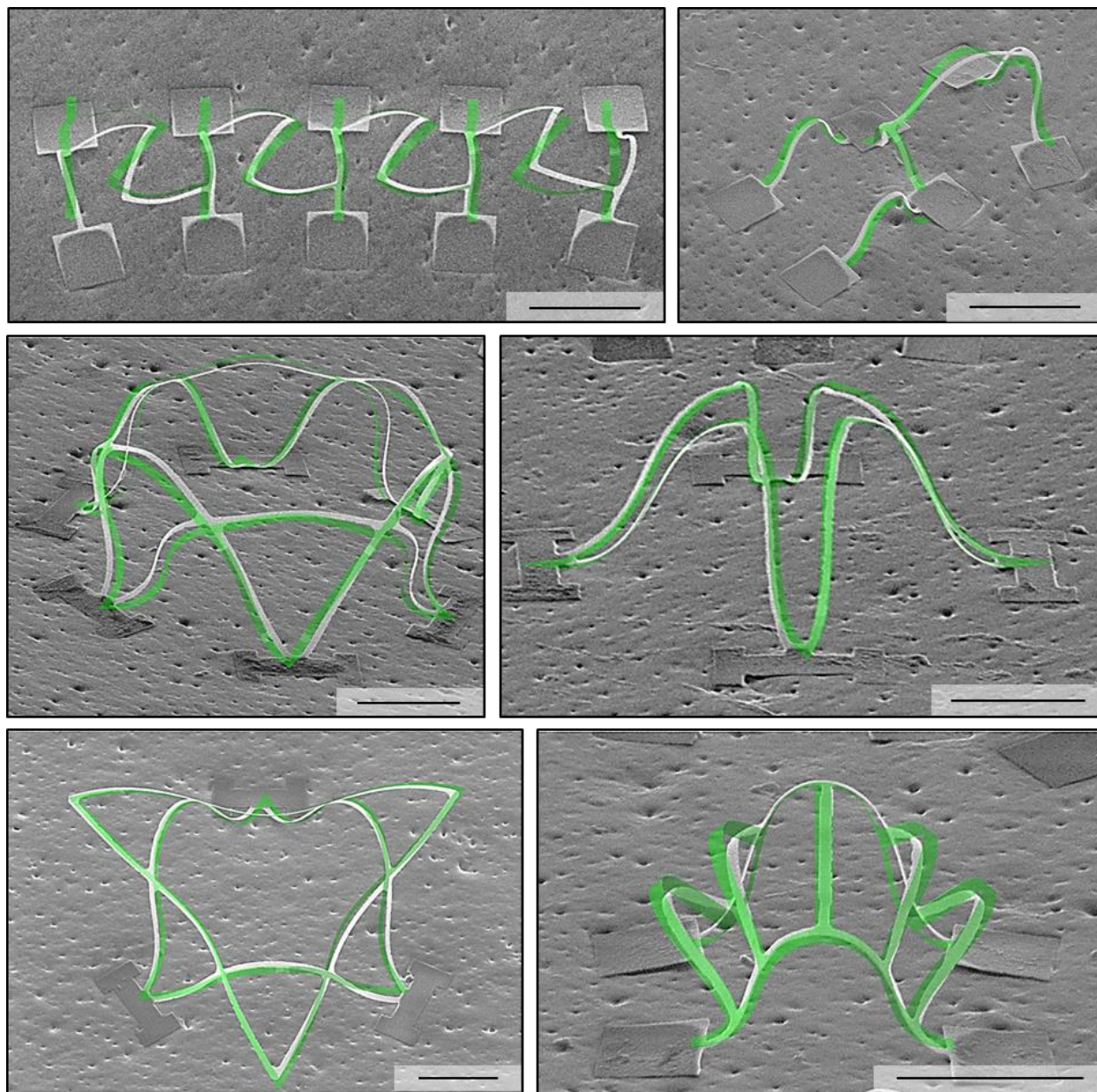
Fig. S16

Experimental images and overlaid FEA predictions of various 3D pop-up structures made from SU8. The scale bars in all images are 500 μm.
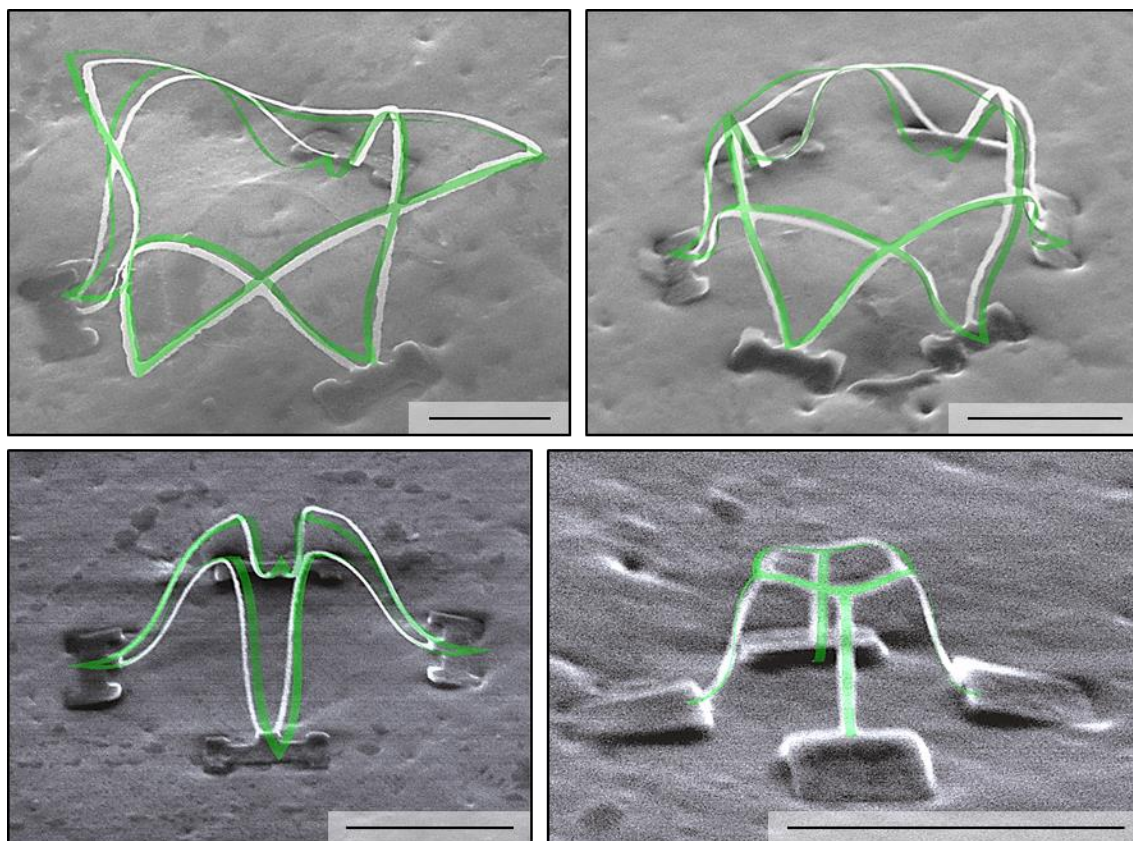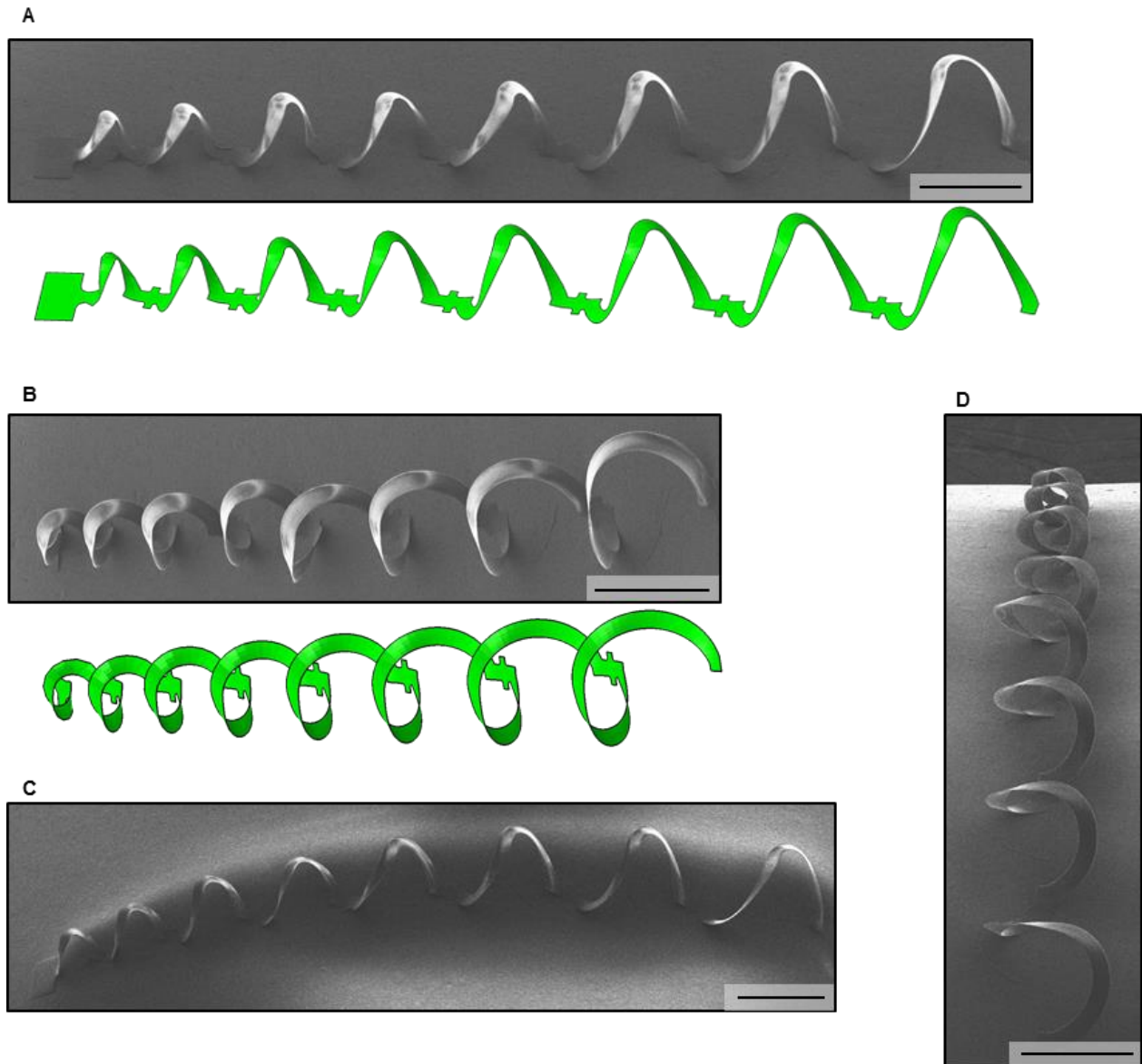
Fig. S17

Experimental images and overlaid FEA predictions of various sub-microscale 3D pop-up structures made from Si. The ribbon width is ~ 800 nm and the ribbon thickness is ~ 100 nm. The scale bars in all images are 15 μm.

Fig. S18

Experimental images and overlaid FEA predictions of various small-scale 3D pop-up structures made from Si. The ribbon width is ~ 3 μm and the ribbon thickness is ~ 300 nm. The scale bars in all images are 50 μm.

Fig. S19

Mechanical bending of the as-fabricated structures. (**A**) and (**B**) demonstrate SEM images and FEA predictions of a 8-period gradient SU8 coil on a planar surface. (**C**) and (**D**) provide SEM images of the same sample in (A) and (B), which is conformally placed on a curvilinear pen surface, with a bending radius of 5 mm. The scale bars in all images are 400 μm.
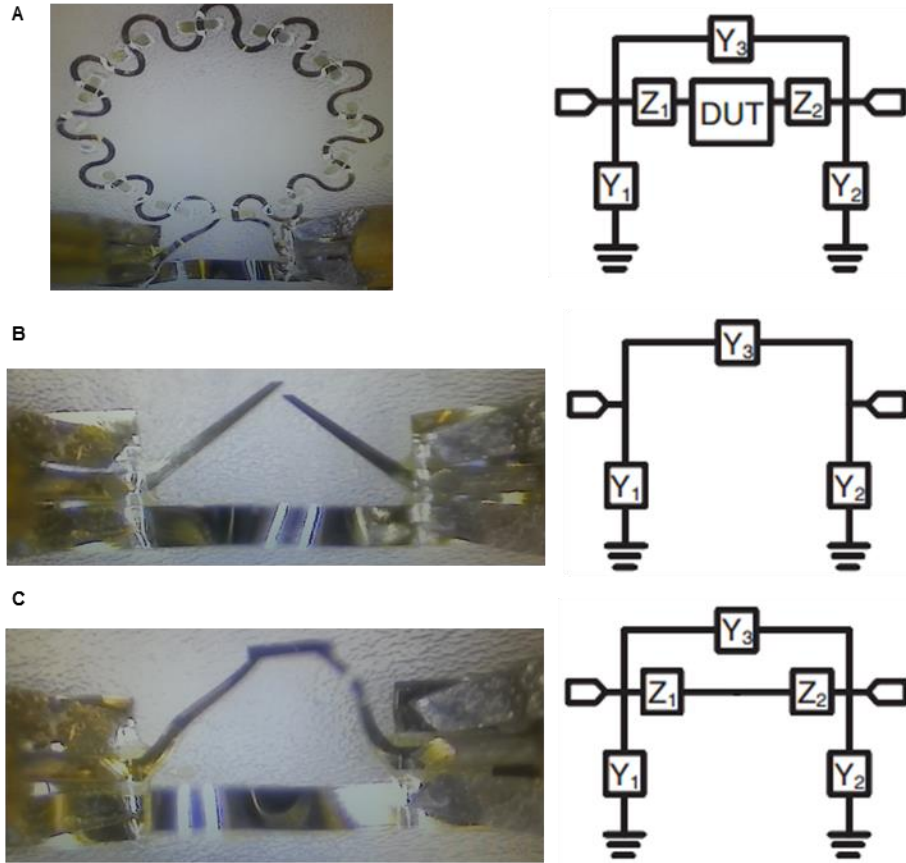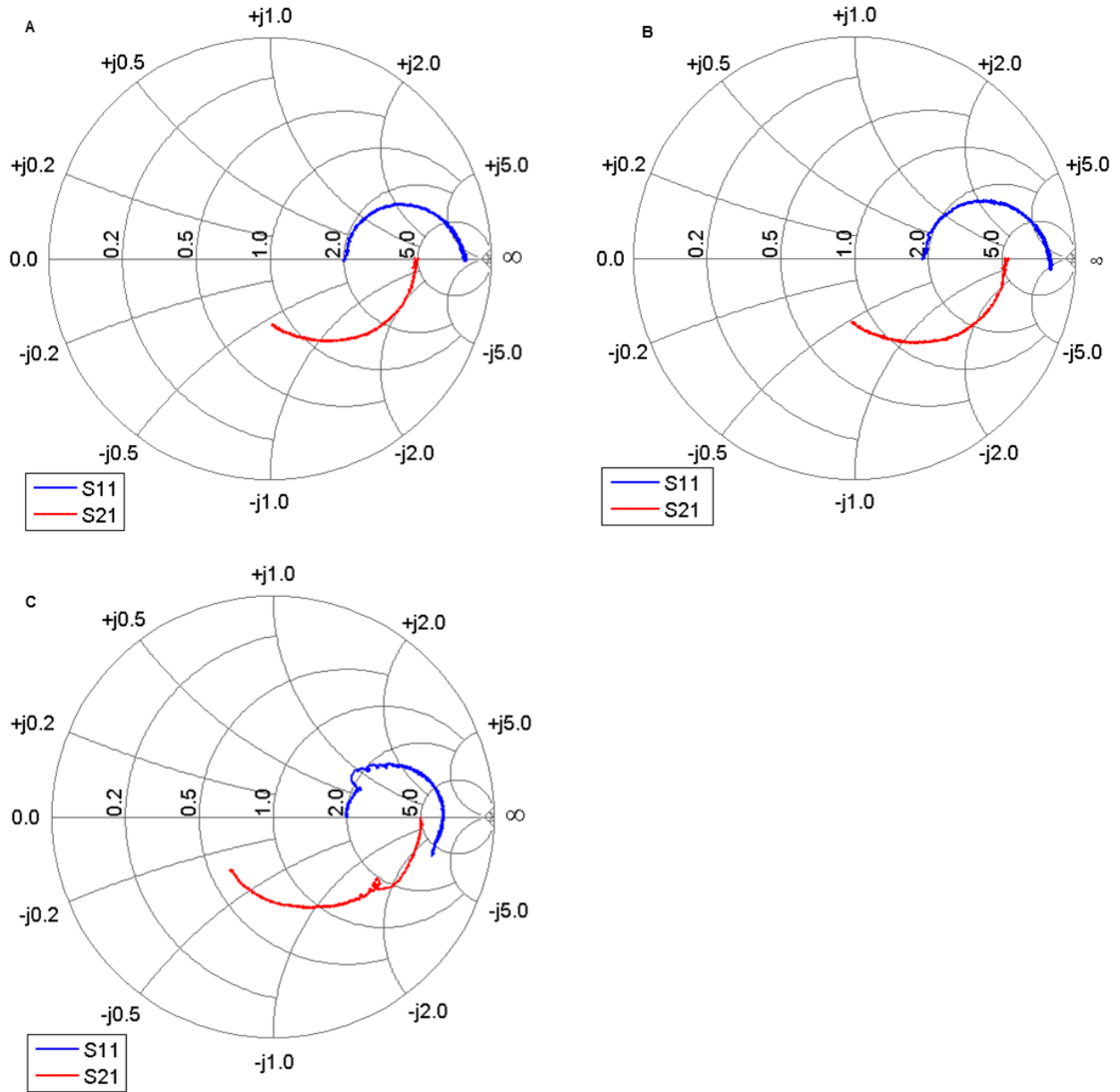
Fig. S20

Open-through de-embedding patterns on an elastomer substrate for popped-up cage inductor RF measurement and their corresponding lumped equivalent circuits. (**A**) Test pattern with the device under test (DUT). (**B**) Open pattern. (**C**) Short pattern.
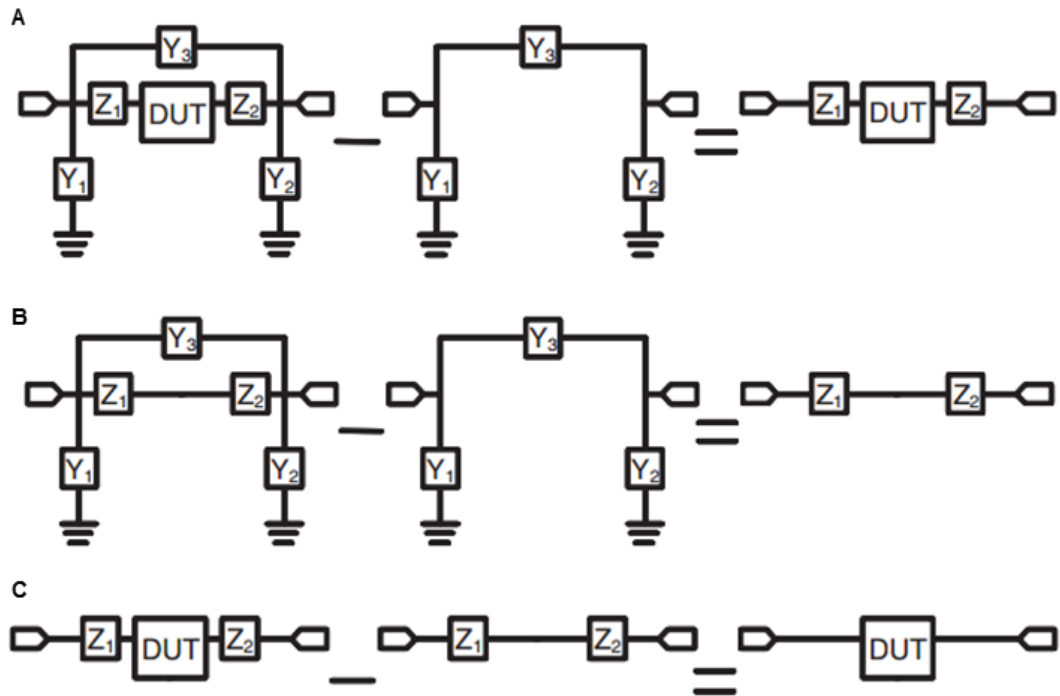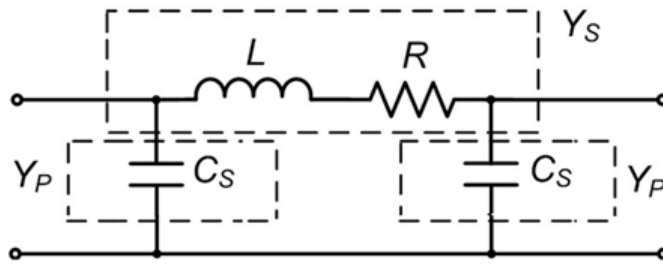
Fig. S21

Mathematic procedure to do the open-through de-embedding. (**A**) Subtract measured data of open pattern from raw data with DUT. (**B**) Subtract measured data of open pattern from data of through pattern. (**C**) Subtract data obtained from step 2 from data obtained from step 1.

Fig. S22

Measured data between 10 MHz and 10 GHz from 3D toroidal samples formed with different substrate prestrain levels. (A) 54%, (B) 33% (i.e. partial release of 54%), and (C) 0%.

Fig. S23
Lumped equivalent circuit of cage inductor on an elastomer substrate.